Corrosion Performance of Ceramic Coatings Based on SiC and $MoSi_2$ on Ni-Based Superalloy for Iodine Sulfur Cycle for Hydrogen Production

By

Zain Hussain

Reg. No: 00000319704

Session 2019-2021

Supervisor

Prof. Dr. Zuhair S. Khan

U.S. –Pakistan Center for Advanced Studies in Energy (USPCAS-E)
National University of Sciences and Technology (NUST)
H-12, Islamabad 44000, Pakistan

March 2022

Corrosion Performance of Ceramic Coatings Based on SiC and $MoSi_2$ on Ni-Based Superalloy for Iodine Sulfur Cycle for Hydrogen Production

By

Zain Hussain

Reg. No: 00000319704

Session 2019-2021

Supervisor

Prof. Dr. Zuhair S. Khan

A Thesis Submitted to U.S. – Pakistan Center for Advanced Studies in Energy in partial fulfillment of the requirements for the degree of

MASTERS of SCIENCE

in

THERMAL ENERGY ENGINEERING

U.S.– Pakistan Center for Advanced Studies in Energy (USPCAS-E)

National University of Sciences and Technology (NUST)

H-12, Islamabad 44000, Pakistan

March 2022

THESIS ACCEPTANCE CERTIFICATE

Certified that final copy of MS thesis written by Mr. Zain Hussain, (Registration No. 319704), of U.S.-Pakistan Center for Advanced Studies in Energy (USPCAS-E), NUST has been vetted by undersigned, found complete in all respects as per NUST Statues/Regulations, is within the similarity indices limit and is accepted as partial fulfillment for the award of MS degree. It is further certified that necessary amendments as pointed out by GEC members of the scholar have also been incorporated in the said thesis.

Signature: _____

Name of Supervisor: Prof. Dr. Zuhair S. Khan

Date: _____

Signature (HoD TEE): _____

Date: _____

Signature (Principal/Dean): _____

Date: _____

Certificate

This is to certify that work in this thesis has been carried out by **Mr. Zain Hussain** and completed under my supervision in Advanced Energy Materials and Systems Laboratory, USPCAS-E, National University of Sciences and Technology, H-12, Islamabad, Pakistan.

Supervisor: _____

Prof. Dr. Zuhair S. Khan
U.S.-Pakistan Centre for Advanced Studies in Energy
NUST, Islamabad

GEC member 1: _____

Dr. Majid Ali
U.S.-Pakistan Centre for Advanced Studies in Energy
NUST, Islamabad

GEC member 2: _____

Dr. Asif Hussain Khoja
U.S.-Pakistan Centre for Advanced Studies in Energy
NUST, Islamabad

GEC member 3: _____

Dr. Mustafa Anwar
U.S.-Pakistan Centre for Advanced Studies in Energy
NUST, Islamabad

HOD-TEE: _____

Dr. Majid Ali
Department of Thermal Energy Engineering
NUST, Islamabad

Principal: _____

Prof. Dr. Adeel Waqas
U.S.-Pakistan Centre for Advanced Studies in Energy
NUST, Islamabad

Acknowledgments

All praise to Allah Almighty who gave me the strength and knowledge to do the work presented in this thesis.

I would like to express my sincere gratitude to my research supervisor, Prof. Dr. Zuhair S. Khan for letting me be part of the research group at Advanced Energy Materials Lab, USPCAS-E, NUST, Islamabad. I feel privileged to have worked under his kind Supervision. It's the blend of his patience, persistence, guidance, and motivation that made me accomplish my research aims in due time. He polished my research skills and I have learned a lot under his supervision and guidance.

I would also like to thank the members of my GEC committee, Dr. Majid Ali, Dr. Asif Hussain Khoja, and Dr. Mustafa Anwar who honored my committee's presence. I would like to sincerely thank my senior Mr. Nisar Ahmad, my fellows, and friends for their unconditional support. Especially, I pay gratitude to Lab Engineers Mr. Asghar Ali, Mr. Aamir Satti, and Mr. Qamar-ud-din for their unmatchable support during the whole research work.

I gratefully acknowledge the financial support provided by the Research and PGP Directorates of USPCASE/NUST.

Abstract

In this era, renewable energy technologies are suitable to meet the challenges of fossil fuel depletion and global warming. Thus, hydrogen fuel is gaining attention as an alternative clean fuel source that can be produced from various methods, one of them is the iodine-sulfur (IS) cycle that is a thermochemical process. One of the important components in the IS cycle is a process heat exchanger (PHE) which requires excellent mechanical properties at an elevated temperature as well as a high corrosion resistance in SO_2/SO_3 environment. In this work, Hastelloy X (HX) superalloy was chosen as a structural material for the sulfuric acid decomposition stage due to its excellent mechanical strength and oxidation resistance at high temperatures. However, HX cannot withstand high-temperature SO_2/SO_3 environments. Therefore, applying a protective coating is a viable option. For that purpose, silicon carbide (SiC) is a potential material that can tolerate this harsh environment but there is a difference in the coefficient of thermal expansion (CTE) of SiC and HX. The CTE of molybdenum disilicide ($MoSi_2$) lies between SiC and HX and it also has high oxidation resistance. Hence, $MoSi_2$ can be utilized as an interlayer between SiC and HX. Herein, $MoSi_2$ and SiC films were deposited via physical vapor deposition methods. In other configurations, SiC was also fabricated through low-cost methods such as the dip-coating technique. Corrosion tests of bare HX and coated samples were performed at different temperatures (60℃, 120℃, and 300℃) in 98% sulfuric acid via the weight-loss method. Furthermore, the corrosion behavior of bare HX, $MoSi_2$ coated HX, SiC coated HX (dip coated), and SiC/$MoSi_2$ coated HX were analyzed through SEM, AFM, FTIR, and XRD. Bare HX exhibited minute weight change and hence, low corrosion rate at low temperature (60℃ and 120℃). However, at high temperatures (300℃) the corrosion rate increased significantly. $MoSi_2$ coating displayed minute weight change as the corrosion resistance of $MoSi_2$ coated HX improved by 48% as compared to bare HX at 120℃. The corrosion resistance of SiC coated HX improved by 97% in comparison to bare HX at 120℃, which considers it sustainable for corrosion protection against sulfuric acid. SiC/$MoSi_2$ coated HX exhibited the best corrosion rate at 300℃. Optical micrographs revealed that both $MoSi_2$ and SiC/$MoSi_2$ coatings remained intact after corrosion at high temperatures. SEM results revealed that there were coalescent particles on the surface of the MoSi2 coated substrate after being immersed in 98% sulfuric acid at 60℃. Moreover, no voids or microcracks were

observed for 60℃ and 120℃. This work demonstrates that SiC coated HX with $MoSi_2$ interlayer can be an aspiring candidate to be utilized as a corrosion-resistant layer for IS cycle.

Keywords: *Ceramic coatings**,** Hastelloy X, Iodine-Sulfur cycle, corrosion resistance*

Table of Contents

List of Figures

List of Tables

List of Journal/Conference Papers

1. “Corrosion Behavior of $MoSi_2$ Coated Hastelloy X for Iodine -Sulfur Cycle for Hydrogen Production”, Zain Hussain[1], Zuhair S. Khan*, Asghar Ali, Nisar Ahmed, Wajahat Qasim, Altamash Shabbir, Key Engineering Materials, Scientific.net ISSN: 1662-9795. **(Under Review)**

List of Abbreviations

GHG	Green House Gasses
PVD	Physical vapor deposition
PAEC	Pakistan Atomic Energy Commission
HTGR	High Temperature Gas-cooled Reactor
I-S	Iodine-Sulfur
SRM	Steam Reforming of Methane
CSP	Concentrated Solar Power
GWP	Global Warming Potential
LCA	Life Cycle Analysis
H_2SO_4	Sulfuric Acid
TBC	Thermal Barrier Coating
GTAW	Gast Tungsten Arc Welding
GMAW	Gas Metal Arc Welding
$MoSi_2$	Molybdenum Disilicide
SiC	Silicon Carbide
CVD	Chemical Vapor Deposition
CTE	Coefficient of Thermal Expansion
EBPVD	Electron Beam Physical Vapor Deposition
RF	Radio Frequency
DC	Direct Current
XRD	X ray Diffraction

AFM	Atomic Force Microscopy
SEM	Scanning Electron Microscopy
FTIR	Fourier Transform Infrared Spectroscopy
HV	High Voltage
E	Energy
B	Magnetic field
E	Electric Field
F	Force
v	Velocity
PID	(Proportional, Integrative, Derivative)
IR	Infrared
HX	Hastelloy X

Chapter 1

Introduction

1.1 Background

In the recent century, the world's population has increased at a higher rate than it has ever before. Our living conditions have greatly improved as a result of scientific advancements, which have resulted in an increase in energy demand. Humans have a natural tendency to seek simple and cost-effective energy sources to suit their needs. Humans have primarily relied on fossil fuels for the past 12 decades because they were the most cost-effective and easiest to obtain. Coal power plants provide the majority of electric electricity, while crude oil derivatives provide transportation. However, things were not as simple as they appeared [1]. Not only are those fossil fuel sources dwindling, but mankind is also paying a high price for climate change caused by carbon dioxide emissions. These significant environmental concerns have forced humanity to seek out environmentally friendly energy sources. One of them is solar, wind, biomass, hydropower, and fission-based nuclear power plants. Those technologies are gaining traction around the world. Renewable energy sources now meet the majority of the world's electricity demand. However, because of their limited availability and ever-increasing energy consumption, we have been forced to develop the most modern energy technology [2].

It is clear that Pakistan is not a poor country in terms of natural resource accessibility, but it is a country that lags in terms of governance. It is alarming to learn that around 15% of the population lacks access to electricity. Energy scarcity is currently causing a slew of problems, and the current situation necessitates understanding not only energy challenges but also human progress, which are inextricably related.

One of the answers to these questions is advanced power generating technologies, such as hydrogen-based new assets for Fusion reactors. In this system, Pakistan has officially established the Nation Tokamak Program, which will require a

lot of hard work to get it ready to start producing energy in the not-too-distant future, and this examination is a step in the right direction [3].

Hydrogen in its basic form is not readily found on Earth. It can, however, be made from molecules available in natural and industrial sources. Hydrogen, although being the lightest element, has the largest energy content per unit mass of any fuel.

The widespread use of hydrogen as a fuel would result in a multifold increase in production capacity. The amount of energy required to produce hydrogen is always larger than the amount of energy produced by hydrogen. As a result, both energy and feedstock will be required to obtain hydrogen. Given global energy consumption levels and the negative environmental effects of current fossil-based energy sources, renewable energy sources are appropriate for long-term hydrogen production.

1.2 Problem statement

One of the main challenges in developing an effective sulfuric acid decomposition process is identifying suitable constitutive materials that can withstand aggressive and high-temperature environments. Recent research has implied that silicon-based ceramics exhibited high corrosion resistance in SO_2/SO_3 environments at elevated temperatures However, their usage is limited because to their brittleness, difficulties in manufacturing, and sudden breakdown under severe thermal stress [4]. Furthermore, the usage of ceramics raises the issue of sealing between metal and ceramic components under different temperature settings. Another material that showed good corrosion resistance was Teflon, but it is only applicable to temperatures up to 300 °C [5]. Meanwhile, metals showed corrosion in this highly corrosive environment [6]. Due to these problems, the use of ceramics coating that are corrosion resistant combined with superalloys have excellent mechanical strength at high temperature were studied to resolve the manufacturability and high-temperature corrosion issue in this work.

1.3 Research hypothesis

In this work, Hastelloy X superalloy was chosen as a structural material for the sulfuric acid decomposition stage due to its excellent mechanical strength and oxidation resistance at high temperatures [7, 8]. However, Hastelloy X cannot withstand high-temperature SO_2/SO_3 environments. Therefore, applying a protective

coating is a viable option. For that purpose, silicon carbide (SiC) is a potential material that can tolerate this harsh environment but there is a difference in the coefficient of thermal expansion (CTE) of SiC and Hastelloy X [9]. The CTE of molybdenum disilicide ($MoSi_2$) lies between SiC and Hastelloy X and it also has high oxidation resistance [10]. Hence, $MoSi_2$ can be utilized as an interlayer between SiC and Hastelloy X.

1.4 Objectives of the Study

The research presented in this thesis focuses on the enhancement of the corrosion resistance of Hastelloy X for the process heat exchanger to be utilized in the I-S cycle. The main topics of this research are deposition of $MoSi_2$ via EBPVD, SiC deposition via RF magnetron sputtering, and corrosion testing at low and high temperatures. The main objectives of this research study are:

- To deposit $MoSi_2$ via Electron Beam Physical Vapor Deposition (EB PVD).
- To Deposit SiC through RF Magnetron Sputtering.
- To deposit SiC in a cost-effective method via Dip Coating.
- Conducting corrosion resistance experiments at low and high-temperature sulfuric acid.
- To improve the corrosion resistance of Hastelloy X against corrosive sulfuric acid by applying silicon-based ceramic coatings.
- To encourage the need for research for future energy sources.

1.5 Scope of the study

Hastelloy X was cut into different dimensions using the low-speed diamond saw cutter. The prepared substrates were cleaned using ethanol and acetone. $MoSi_2$ source of 99.99% purity was used as target material for EBPVD onto Hastelloy X. The substrate temperature was set at 200℃ and sample rotation speed to 10 rpm. Moreover, a base pressure of 2×10^{-6} Torr was achieved for this coating process. The deposition rate was kept at 1.08Å/s by alternating the current. Surface morphology and topography were characterized by scanning electron microscopy (SEM) and atomic force microscopy (AFM), respectively. In the second part, RF magnetron sputtering was used to deposit SiC thin film on graphite. The substrate temperature was increased up to 300°C. Moreover, substrate rotation speed was kept at 10 RPM. The gas pressure

of 3 Pascal was used along with RF power of 120 W. 900 nm Silicon carbide thin film was deposited in 2 hours. SiC slurry was prepared using the oxidized SiC powders along with PEG as a binder. Both the immersion and withdrawal speeds were set to 35mm/min. The sample stayed inside the solution for 30 seconds. This process was repeated five times and then the coated samples were dried at 100℃ in a drying oven. Surface morphology and structural analysis were characterized by Optical Microscopy (OM) and FTIR. Corrosion testing was carried out at both low and high temperatures. For low-temperature testing, the samples were immersed in 98% sulfuric acid at 60℃ and 120℃. The corrosion rate was measured using the weight loss method. The samples were weighed before and after the corrosion to measure weight loss. A new setup was devised for high-temperature corrosion testing. The sample was immersed in 98% sulfuric acid which was then brought to boiling temperature. The sample was placed inside a round bottom flask which was covered in glass wool and wrapped inside an electric heater. The heater has a maximum temperature limit of 500℃. The steps of this research scope are shown in Figure 1-1.

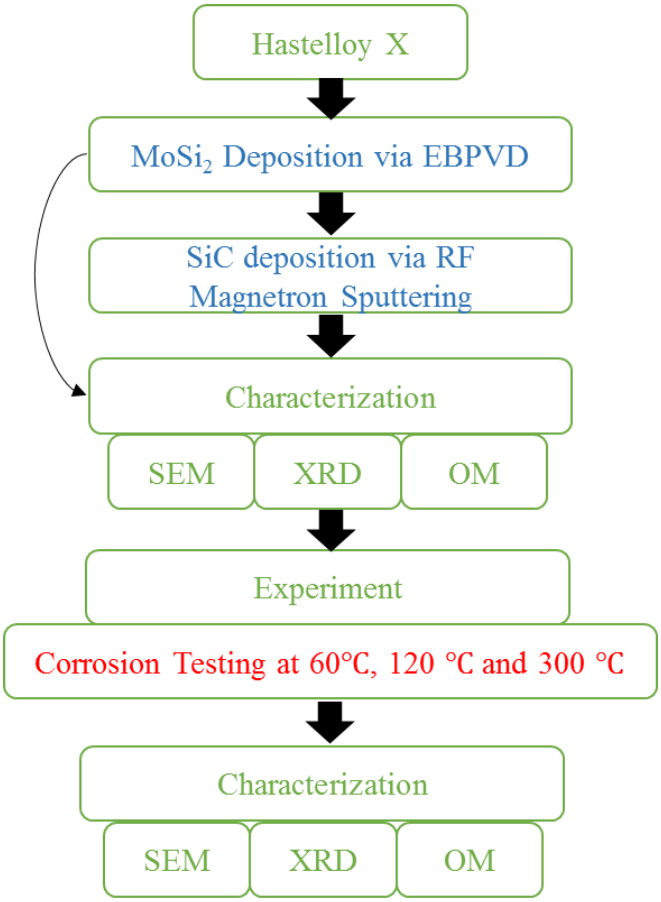

Figure 1-1 Steps involved in the research scope.

1.6 Flowchart of thesis

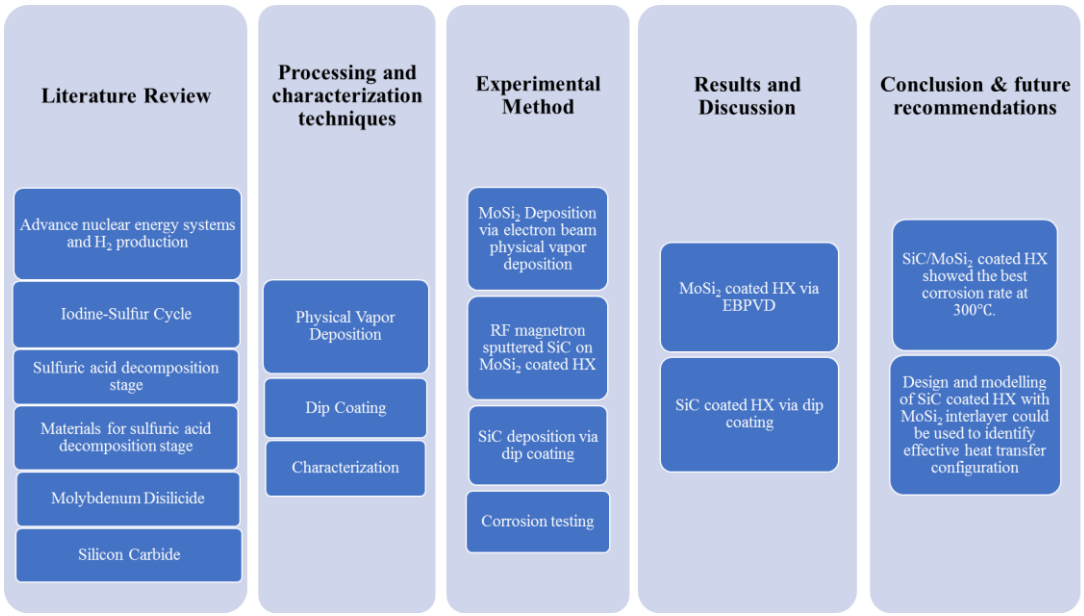

Figure 1-2 Flow chart of thesis.

References

1. Rehman, A., et al., *The effect of carbon dioxide emission and the consumption of electrical energy, fossil fuel energy, and renewable energy, on economic performance: evidence from Pakistan.* 2019. **26**(21): p. 21760-21773.
2. Wang, Z., B. Zhang, and B.J.J.o.c.p. Wang, *Renewable energy consumption, economic growth and human development index in Pakistan: evidence form simultaneous equation model.* 2018. **184**: p. 1081-1090.
3. Maqbool, R. and Y.J.J.o.c.p. Sudong, *Critical success factors for renewable energy projects; empirical evidence from Pakistan.* 2018. **195**: p. 991-1002.
4. Park, J.-W., et al., *Materials development for process heat exchanger (PHE) in nuclear hydrogen production system.* Nuclear Engineering and Design, 2014. **271**: p. 318-322.
5. Barry, P.R., et al., *Effect of Temperature on the Friction and Wear of PTFE by Atomic-Level Simulation.* Tribology Letters, 2015. **58**(3): p. 50.
6. Connolly, S.M., et al., *Design of a composite sulfuric acid decomposition reactor, concentrator, and preheater for hydrogen generation processes.* International Journal of Hydrogen Energy, 2009. **34**(9): p. 4074-4087.
7. Aghaie-Khafri, M., N.J.M.S. Golarzi, and E. A, *Forming behavior and workability of Hastelloy X superalloy during hot deformation.* 2008. **486**(1-2): p. 641-647.
8. Wang, F.J.T.I.J.o.A.M.T., *Mechanical property study on rapid additive layer manufacture Hastelloy® X alloy by selective laser melting technology.* 2012. **58**(5): p. 545-551.
9. Park, J.-W., et al., *A surface modification of Hastelloy x by a SiC coating and an ion beam irradiation for a potential use for iodine-sulfur cycle in nuclear hydrogen production system.* 2008. **1125**.
10. Govindarajan, S., et al., *Synthesis of molybdenum disilicide on molybdenum substrates.* 1995. **76**: p. 7-13.

Chapter 2

Literature Review

2.1 Hydrogen as Alternative fuel Source

Hydrogen is the most abundant element found in the universe accommodating for about 75% of all matter. H_2 is available on Earth in the forms of compounds but not in basic form. Inside earth's crust, it is the 10^{th} most abundant element found with other elements in the form of compounds. The free from of H_2 is not present in earth's atmosphere due to earth's low gravitational pull in comparison to Jupiter and Saturn to maintain lightweight H_2 molecules. According to scientists, H_2 and He were the 1^{st} elements to originate during the dormant period of cosmic history.

Hydrogen has three isotopes present in the Earth's atmosphere namely protium, deuterium, and tritium. Protium is the most basic element and the major component of hydrogen. It is made up of one proton and one electron. Even though, H_2 is lightweight, but it has excellent specific energy for a fuel.

Hydrogen's widespread use as a fuel would result in a multifold increase in production capacity. The amount of energy required to produce hydrogen is always larger than the amount of energy produced by hydrogen. As a result, both energy and feedstock would be needed to produce H_2. Given global energy consumption levels and the negative environmental effects of current fossil-based energy sources, renewable energy sources are appropriate for long-term hydrogen production [1].

2.2 Advance Nuclear Energy Systems and H_2 Production

Nuclear energy-based hydrogen generation from the water provides a huge and cost-effective amount of hydrogen, enhanced energy security, and environmentally pleasant operation. Thermochemical water-splitting technologies could be used to produce hydrogen utilizing nuclear power plant energy. They can also directly harness the heat produced by nuclear reactors. The iodine–sulfur (IS) process (or sulfur–iodine (SI) process is a thermochemical water-splitting process which comprises of three

stages. This method was first studied by General Atomics which required maximum temperature of around 900 °C to operate. This temperature was achievable by utilizing the heat produced in one of the type of nuclear reactors namely high-temperature gas-cooled reactors (HTGRs). This three-stage reaction is viable due to involvement of less chemical reactions, it could also be thermally efficient and the reactants are regenerated in this process. The materials used in I-S cycle must have excellent corrosion protection due to the corrosive environment generated in the process.

The long-term goal is to industrialize a large-scale hydrogen generation system based on the IS process and HTGRs. One of the most important engineering jobs in achieving this is screening and selecting structural materials for chemical reactors that are resistant to the corrosive conditions in which the processes take place.

Due to its zero-carbon emissions, hydrogen is one of the most promising and feasible alternatives to fossil fuels [2, 3]. It can be produced by various processes like steam reforming, electrolysis, and thermochemical water-splitting. The overall efficiency of the electrolysis process is between 20-25% [4]. Meanwhile, the overall efficiency of thermochemical cycles is expected to be between 40-50%. One of the promising and clean methods is the Iodine-Sulfur cycle which is a thermochemical process. Normally, water splits into hydrogen and oxygen thermally at around 4500K but in this process, these products are achieved at around 1200K in the presence of a catalyst [5]. The amount of heat required can be supplied by a nuclear source or solar thermal source which are green resources [4, 6]. General Atomic was the one who originally proposed this cycle [7]. They proposed it for nuclear applications initially. This cycle consists of three stages namely the Bunsen stage, Sulfuric acid decomposition stage, and HI decomposition stage.

The Iodine-Sulfur cycle is a three-step thermochemical reaction that is used to produce hydrogen. In this cycle, the net reactant is water and the net products are hydrogen and oxygen. Meanwhile, all other chemicals are regenerated in this cycle. The first step is called the Bunsen reaction which occurs between 20-120℃. For azeotropic mixture, the optimum temperature range for this reaction is between 72-87℃ [8].

2.3 Production of Hydrogen from Various Methods

2.3.1 Steam reforming

Hydrogen production systems based on fossil fuels have developed mature technology with improved efficiency and lower output costs. Natural gas (NG) is mainly methane, and the SMR (steam reforming of methane) method is frequently used to produce hydrogen from natural gas, with a 65–75 percent efficiency range. The partial oxidation of NG is effective method for hydrogen production and it has almost 50% efficiency [9]. The premier coal gasification technology can harvest up to 97% pure hydrogen by Koppers-Totzek process. The carbon sequestration and solar thermal technologies are able to produce fossil fuel based H_2 that may use in the short and medium future [10].

2.3.2 Electrolysis

Water electrolysis efficiency levels might range from 70 to 90 percent. Various PV electrolysis plants are in operation all around the world. The electricity generated from wind or concentrated solar power (CSP) can also be used for electrolysis. Electrolysis processes fueled by electricity from renewable energy sources have a low global warming potential (GWP), less than 5 kg CO_2 eq/kg H_2, according to life cycle analysis (LCA) research, with wind energy powered electrolysis have a lowest GWP. The GWP of electrolysis utilizing grid energy can generate 30 kg CO_2 eq/kg H_2 [10].

2.3.3 Direct and Indirect Biophotolysis

Biohydrogen generation with (micro) organisms [11] is a newer subject that includes photo and dark fermentation, indirect and direct biophotolysis of water, and bacterial microbial electrolysis of organic materials. Biophotolysis is the mechanism by which some microorganisms, such as cyanobacteria and green algae, produce H_2 by consuming and splitting water in their normal metabolic processes through sunlight [12]. The organic compound decomposed by photosynthetic process [13]. When the organic material is exposed to Infrared radiation, the purple bacteria (non-sulfur) may produce H_2 by breaking the organic structure of material. In the dark, organic molecules are fermented to produce hydrogen [11] Anaerobic bacteria can degrade organic matter into hydrogen and other chemicals without the use of sunlight. As bacteria break down organic material, at the anode of the cell a low voltage is formed

in microbial electrolysis. The integrated systems such as hybrid biohydrogen in which byproducts from one method are used as inputs in another, resulting in H_2 production [14].

2.3.4 Thermochemical Process:

Single-step and multi-step thermochemical hydrogen generation from water are both conceivable. Direct thermal breakdown of water is feasible above 1727 °C. Temperature has a direct effect on the extent of single-step water dissociation (from 1 percent at 1727 °C to 34 percent at 2727 °C). Lowering the pressure has a positive impact on the procedure. The dissociation of water into hydrogen and oxygen is achievable by two or more sequential reaction stages utilizing redox elements such as Sulphur and certain metal oxides, and hydrogen can be created at relatively lower temperatures through thermochemical cycles. In comparison to metal oxide cycles, sulfur-based cycles can run at lower temperatures (927 °C). There have been nearly 2000–3000 thermochemical cycles explored, with 20–30 of them potentially appropriate for large-scale hydrogen production. Thermochemical cycles can achieve efficiency levels of up to 40%–50%. H_2SO_4 single bond I_2, H_2SO_4 single bond HBr, $CaBr_2$ single bond Fe_2O_3 (UT-3), and $FeCl_2$ (Mark 9) cycles are a few instances [15]. Thermochemical technologies are appropriate for capturing high-temperature solar energy in CSP systems [16] and nuclear heat [17].

Light-driven photobiological processes can be used to release hydrogen from water [22], photochemical [18], and photoelectrochemical systems [19]. These approaches are still in the early stages of development, and their efficiency is currently quite low. However, there is still hope for a breakthrough through the discovery of novel catalytic materials.

Metal hydride pyrolysis and hydrolysis can be used to produce hydrogen. Lithium and magnesium hydride (LiH, MgH_2), lithium and sodium borohydride ($LiBH_4$, $NaBH_4$), and lithium and sodium aluminum hydride ($LiAlH_4$, $NaAlH_4$) are all examples of lithium and magnesium hydrides [20].

2.3.4.1 Iodine Sulfur Cycle

The Iodine-Sulfur cycle is a three-step thermochemical reaction that is used to produce hydrogen. In this cycle, the net reactant is water and the net products are hydrogen and oxygen. Meanwhile, all other chemicals are regenerated in this cycle. The first step is called the Bunsen reaction which occurs between 20-120℃ as illustrated in Eq. 2-1. For azeotropic mixture, the optimum temperature range for this reaction is between 72-87℃ [8].

$$I_2 + SO_2 + 2H_2O \rightarrow 2HI + H_2SO_4 \qquad \text{Eq. 2-1}$$

Sulfuric acid is decomposed into SO_2, this stage is called the sulfuric acid decomposition stage. This stage occurs at 830-900℃ as shown in Eq. 2-2 [21].

$$H_2SO_4 \rightarrow SO_2 + {}^{1}/_{2}\, O_2 + H_2O \qquad \text{Eq. 2-2}$$

At above 350℃ sulfuric acid decomposes into SO_3 and H_2O without the help of a catalyst. But to convert SO_3 into SO_2 a catalyst is required with a temperature above 850℃ [22].

The HI is separated by distillation (Liquid-Liquid separation). HI is then decomposed into hydrogen and iodine. This reaction occurs at 300-450℃ as given in Eq. 2-3 [21].

$$2HI \rightarrow H_2 + I_2 \qquad \text{Eq. 2-3}$$

This stage produces hydrogen which is to be used as a fuel source. Meanwhile, I_2 is recycled which can be used in the Bunsen reaction stage again. The process diagram of the I-S cycle is shown in Figure 2-1.

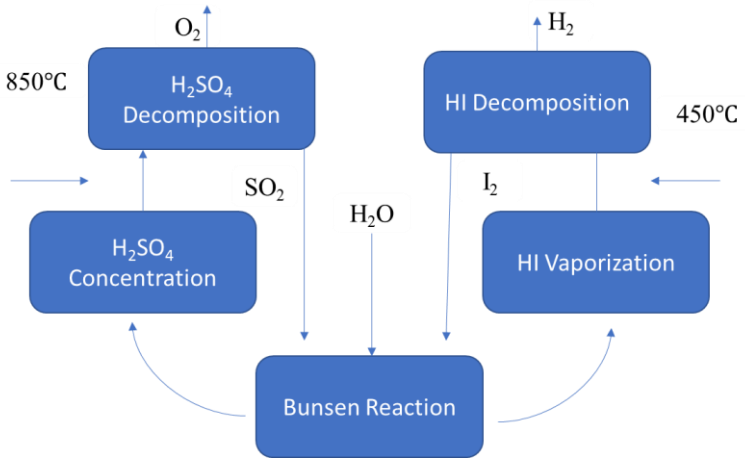

Figure 2-1 Process diagram of Iodine-Sulfur cycle [23].

2.3.4.1.1 Sulfuric Acid Decomposition

As discussed in the previous section, the second stage is the sulfuric acid decomposition stage in which the temperature reaches around 900℃. This stage occurs in two steps i.e. in the first step sulfuric acid decomposes into Sulphur trioxide gas and releases steam at temperatures above 300℃. This step is shown in Eq. 2-4 [24].

$$H_2SO_4 \rightarrow SO_3 + H_2 \qquad \text{Eq. 2-4}$$

In the 2nd step, this SO_3 gas is converted into SO_2 and oxygen at around ~900℃ in the presence of a catalyst. The SO_2 produced is used in the Bunsen stage and oxygen is the by-product as shown in Eq. 2-5.

$$SO_3 \rightarrow SO_2 + 1/2O_2 \qquad \text{Eq. 2-5}$$

Normally, the acid in the liquid phase is much more corrosive than the gaseous phase because of a few driving factors. The temperature and concentration of the acid drive the corrosion behavior of aqueous sulfuric acid. At room temperature and concentration below 85 wt%, sulfuric acid behaves as a reducing agent. Also, at high temperatures and concentrations below 65 wt%, H_2SO_4 behaves as a reducing agent. But at high temperatures and high concentrations sulfuric acid behaves as an oxidizing agent. So, the selected structural materials will have to counter both oxidizing and reducing environments. Tantalum and Gold showed good resistance against highly concentrated H_2SO_4 environments. Meanwhile, platinum and gold showed complete

resistance against all concentrations of sulfuric acid. But due to their high cost and low yield, they have considered corrosion-resistant coatings [25].

Because of a few variables, a liquid environment is far more corrosive than a gaseous environment. The driving force of all corrosion processes, ion transport, is substantially stronger in the liquid phase, boosting the corrosion redox reaction. In a gaseous atmosphere, the corrosion product will most likely remain on the reaction surface and may function as a barrier, limiting further reaction. Flowing liquid chemicals, on the other hand, can dissolve and/or eliminate such corrosion products, resulting in increased corrosion. The H_2SO_4 concentration stage provides a difficult corrosion challenge. This is due to the fact that the corrosion mechanism of liquid H_2SO_4 is temperature and acid concentration dependent. In nature, H_2SO_4 is decreasing when the acid concentration is less than 85 wt percent at room temperature or less than 65 wt percent at higher temperatures. It becomes an oxidizing agent at high concentrations and temperatures. As a result, building materials for acid concentration applications will be exposed to both oxidizing and reducing environments. Ta and Au corrode slowly in higher concentration H2SO4 liquid phase conditions. Precious metals such as Au and Pt have demonstrated perfect resistance to H2SO4 at all concentrations. However, because to their intrinsic high cost and poor yield strength, they are only practicable as corrosion-resistant coatings or cladding for components. Techniques for applying precious metals coating on a base structure are widely accessible, but care must be taken to address intrinsic flaws such as pinholes, which might jeopardize the component's integrity. [25].

2.3.4.1.2 Problems faced in the I-S cycle

The main challenges in developing an effective sulfuric acid decomposition process are (1) identifying suitable constitutive materials that can withstand aggressive and high-temperature environments; (2) identifying high-performance catalytic materials that can achieve the high activity, reduced degradation, and low costs for large-scale hydrogen production; and (3) identifying effective heat transfer configurations.

Oxidation is a corrosion process that happens in gaseous conditions to metal alloys, resulting in the creation of an oxide layer on the metal's outer surface. At high

temperatures, most metals, including superalloys typically employed in gas turbine applications, are prone to oxidation. Surface cracking, spallation, erosion, and depletion of alloying elements are all examples of how oxidation may decrease the performance of superalloys. The aerospace industry is investing extensively in developing new superalloys and thermal barrier coatings to improve the oxidation resistance of gas turbine components (TBCs). The following sections go through the oxidation processes, rates, and kinds of oxidation that nickel-based superalloys go through [26].

Temperature is also important in affecting the rate of oxidation of a metal. The rate of oxidation is proportional to temperature, which is known as an Arrhenius relationship. Similarly, it is known that the oxidation rate of pure metals is related to grain size [27]. The transit of metal ions such as Cr, Al, and Si to the metal-oxide interface is hampered when the grain size is reduced, resulting in a reduction in oxidation rate [28].

2.3.4.1.3 Materials for Sulfuric Acid Decomposition Stage

The sulfuric acid decomposition process requires a material that can withstand a harsh acidic environment at high temperatures. Due to this, it is necessary to focus on materials for that section of the Iodine-Sulfur cycle for achieving the required results.

Table 2-1 summarizes the corrosion rate of various materials for the sulfuric acid decomposition stage in the I-S cycle. Corgnel et. al gave a summary of a few materials in their review in which various tests were carried out to test their stability in the sulfuric acid decomposition stage [5]. The materials undergo two tests, one called sulfuric acid vaporization and the other called sulfuric acid decomposition. Eq. 2-4 is the sulfuric acid vaporization stage and Eq. 2-5 is the sulfuric acid decomposition stage. Candidates for structural materials in the sulfuric acid vaporization stage were Incoloy 800H, AL610, high Si steel, Si_3Ni_4, Hastelloy G, and C-276. The set of conditions in this stage was temperature between 350-550℃ in presence of steam, sulfur trioxide, and other contaminants. The tests were conducted for 100h in 95wt% sulfuric acid.

Table 2-1 The corrosion rate of materials.

Sr. No.	Material	Parameters	Corrosion Rate	Ref.
1	Incoloy 800H, SiC and Hastelloy C-276	350-550℃ 100 h in 95 wt% Sulfuric Acid	Incoloy 800H:<5 mm/year SiC:≈ no corrosion Hastelloy C-276:≈1mm/year	[4]
2	Aluminide Coatings	550-950℃ 100 h in 95 wt% Sulfuric Acid	$1mg/cm^2$	[9]
3	SiC and Si_3N_4	320℃, 75 wt% Sulfuric Acid 380℃, 85wt% Sulfuric Acid 460℃, 95 wt% Sulfuric Acid	Both showed no corrosion at 320℃ and 380℃ SiC:-0.10 for 100h and -0.002 for 1000h ($gm^{-2}h^{-1}$) Si_3N_4: no corrosion for 100h and -0.007 for 1000h ($gm^{-2}h^{-1}$)	[10]
4	SS-304, SS-310, SS-316, Inconel-800 and Hastelloy C-276	60℃ & 120℃ in 95-98 wt% Sulfuric Acid	SS-304: 1.95 at 60℃ and 4.46 at 120℃ SS-316: 0.74 at 60℃ and 4.07 at ℃ SS-310: 2.53 at 60℃ and 5.32 at 120℃ Inconel-800: 0.71 at 60℃ and 3.47 at 120℃ Hastelloy C-276: 0.32 at 60℃ and 2.91 at 120℃ (mm/yr)	[11]

Kubo et al. performed immersion tests to examine the corrosion resistance of multiple ceramics and acid-resistant metals for the construction of H_2SO_4 processing equipment inside the I-S cycle. The materials under examination were silicon carbide (SiC), silicon SiC, silicon nitride, high silicone iron (Fe-Si), and Sandvik SX which is a silicon enriched alloy. Tests were conducted under different concentrations and temperatures inside an autoclave. The samples were placed inside quartz ampoules with the presence of 5mL sulfuric acid. Sandvik SX suffered uniform corrosion at 95 wt% H_2SO_4 and was deemed as a failure. Fe-Si showed some corrosion resistance and was rated fair, but it showed evidence of crack formation. Meanwhile, SiC, Si-SiC, and Si_3Ni_4 showed no weight changes and were rated excellent. It was concluded that silicon-containing ceramics showed excellent corrosion resistance against all concentrations of H_2SO_4 (75 wt% to 98wt%) [21].

2.3.4.1.4 Hastelloy X as a structural material for PHE

Hastelloy X is a nickel-based alloy that is widely used in gas turbine combustion components due to its high oxidation resistance at high temperatures. However, when it is subjected to high-temperature sulfuric acid, it begins to corrode. The nominal composition is shown in Table 2-2**.**

Table 2-2 Nominal Composition of Hastelloy X.

Element	Wt%
Nickel	47
Chromium	22
Iron	18
Molybdenum	9
Cobalt	1.5
Tungsten	0.6
Carbon	0.1

Manganese	1
Silicon	1
Boron	0.008
Niobium	0.5
Aluminum	0.5
Titanium	0.15

Hastelloy X is a high-temperature alloy with good oxidation resistance, formability, and heat resistance. The nickel-based solid solution superalloy is commonly utilized for ducts or liners in the combustion stage of gas turbine engines in the aerospace industry. Hastelloy X is regarded as having great weldability and a low risk of cracking. Gast Tungsten Arc Welding (GTAW) or Gas Metal Arc Welding (GMAW) can be used to weld Hastelloy X [29, 30].

A chromia, Cr_2O_3, or alumina, Al_2O_3, oxide layer forms on nickel-based superalloys to protect them from further oxidation. These oxides are responsible for nickel-based superalloys' ability to withstand high temperatures with minimal material loss owing to spallation. There are three types of oxidation behaviors that can occur in Ni-Cr alloys, including Hastelloy X, depending on the amount of Cr in the system.

Alloys having less than 10% Cr concentration are classified as Type I. The rate constant ‘k' in type I alloys, also known as dilute alloys, is just slightly higher than that of pure nickel. Because of the doping of the scale with r, the oxide scale in type I allows for a faster diffusion rate of Ni ions.

Alloys having a Cr concentration of between 10% and 30% are classified as Type II. Chromia develops largely along external grain boundaries in these alloys, with occasional interior chromia occurrences. Furthermore, nickel oxide (NiO) occurs on the outside of alloy grains.

Finally, alloys containing more than 30% Cr are classified as type III. The rate constant k′ in these alloys is several orders of magnitude lower than in pure nickel.

The oxides generated on the surface of wrought Hastelloy X are constituted of two layers: a manganese-rich spinel on the outside layer and Cr_2O_3 on the inner layer, according to studies [31].

2.3.4.1.5 Molybdenum Disilicide as an intermediate layer between SiC and Hastelloy X

Materials based on the silicide $MoSi_2$ have considerable promise for a broad variety of high-temperature structural applications, particularly over 1000°C. Industrial uses include furnace elements and components, power generation components, high-temperature heat exchangers, gas burners, lances for liquid metals and glasses, igniters, and high-temperature filters. Aerospace applications make use of turbine aircraft engine hot-section components such as blades, vanes, combustors, nozzles, and seals. In automotive applications, turbocharger rotors, valves, glow plugs, and advanced turbine engine elements are all employed. [32].

$MoSi_2$ has a unique set of features that make it appealing as a high-temperature material. It has a high melting point of 2030°C and strong high-temperature oxidation resistance, which is virtually similar to that of silicon-based structural ceramics Sic and S&N. It has a brittle-to-ductile transition in the vicinity of 900 "C, as determined by single-crystal compression [33].

$MoSi_2$ is thermodynamically stable in the presence of a wide range of possible ceramic reinforcements for composites, including SiC, S&N, ZrO, Al_2O_3, mullite, YAG, Y203, TiB, and TiC. It is substantially stable across the entire range of significant structural ceramic materials. Another way to improve the characteristics of $MoSi_2$ is to alloy it with additional high melting point silicide materials. WSi, NbSi, CoSi, and Ti, Si, are all possible silicide alloying species. $MoSi_2$ is a non-toxic and environmentally friendly material that is abundant and reasonably inexpensive. $MoSi_2$ and $MoSi_2$-based materials can be electro-discharge machined (EDM) due to their high electrical conductivity [34].

The structural application of $MoSi_2$, materials, can be divided into four categories. The first is as a matrix for composites made of $MoSi_2$. To date, this area has witnessed the most action. The usage of $MoSi_2$ as a reinforcement for structural ceramic-matrix composites is a second aspect. To present, very little study has been

done in this field. Because of its oxidation resistance and high melting point, $MoSi_2$ is a promising high-temperature connecting material for structural ceramics. Finally, $MoSi_2$-based compounds can be used to coat refractory metals and carbon-based materials with oxidation-resistant coatings [35].

The silicide $MoSi_2$ is best defined as a ceramic-intermetallic combination on the edge of ceramicity. A ceramic is a solid, ionocovalent, inorganic compound, according to a general definition. When this definition is applied to $MoSi_2$, it reveals its borderline character, as it varies from a ceramic only in that its atomic bonding is a combination of covalent and metallic. $MoSi_2$ has ceramic-like oxidation resistance at high temperatures and metal-like electrical conductivity. At room temperature, this material exhibits ceramic-like brittleness, therefore fracture toughness is a serious concern. It also exhibits metal-like plasticity at high temperatures, making creep resistance a key concern [36].

2.3.4.1.6 Silicon Carbide as a corrosion-resistant layer

Silicon carbide is commonly thought to be abrasive and heat flux tolerant. SiC's fast saturation electron velocity, wide forbidden band, and superior radiation resistance make it ideal for high-voltage, high-frequency, and high-temperature electronic components and devices. SiC thin films and composites offer a wide range of technological applications in nuclear engineering [37]. Its exceptional hardness and extremely high melting temperatures make it an excellent candidate for high-temperature reactors. Their uses could range from corrosion-resistant coatings to X-ray mask materials to the protection of thermonuclear reactor walls.

The performance of silicon carbide as a protective coating has been studied in several ways. SiC was deposited on an aluminum matrix using a thermal spray method in one investigation. It was also shown that grain size affects it [38]. It was discovered that when grain size grew, corrosion resistance improved. Another work used laser cladding to put silica particles on a graphite substrate [39]. In comparison to bare graphite, the silica covering performs exceptionally well in ablation tests. Chemical vapor deposition (CVD) was used in one study to deposit SiC on graphite. The impact resistance of high-temperature annealing was investigated. The sample impact strength

increases with deposition temperature, peaking at 1150 °C and then declining somewhat at 1200 °C [40].

Because of its low density and CTE, as well as strong thermal conductivity, silicon carbide has been identified as a possible material for use as a protective coating against high-temperature corrosive environments. Silicon carbide with $MoSi_2$ as interlayer onto Hastelloy X via physical vapor deposition. The method was shown to be effective in achieving homogeneous composition and grain structure [41]. Another study used a chemical vapor process to deposit SiC and glassy carbon composite on graphite. It was discovered that a SiC could be a potential protective layer [42].

Summary

With the beginning of the 21st century, energy demand has been increased significantly. Especially in developing countries energy shortage is one of the critical issues. Most of the energy demand in the world is met by fossil fuels. These fuels are not only depleting but Carbon dioxide emission into environmental fuels is producing the greenhouse effect which is increasing global temperature. So, the world is looking for an alternative clean and economical source of energy. Currently, Pakistan is overwhelmingly dependent on fossil fuel resources to meet its energy demand. Another drawback of using these sources is the GHG emissions. One of the alternatives to this problem is using hydrogen as an energy source which can be produced using a renewable source like solar thermal and nuclear energy. Pakistan already has six nuclear reactors operating with full capacity. Hydrogen can be produced from various methods like steam reforming of methane, electrolysis, thermochemical decomposition, or direct and indirect biophotolysis.

In this chapter, we discuss one of the thermochemical processes used for the production of hydrogen named as Iodine-Sulfur cycle. The process operates at a maximum temperature of 900℃ which comprises three stages. The sulfuric acid decomposition stage is discussed in detail due to its high corrosion behavior at high temperatures. Structural materials for the process heat exchanger for this stage are discussed. According to recent research, Silicon-based ceramics showed the best corrosion resistance against boiling sulfuric acid. Hastelloy X is a superalloy that is used in high-temperature applications like the aerospace industry due to its oxidation resistance. But it is not viable against boiling sulfuric acid. SiC is to be coated onto Hastelloy X to improve its corrosion resistance. But there is a mismatch between the coefficient of thermal expansion (CTE) between SiC and Hastelloy X. $MoSi_2$ is a potential candidate to act as an intermediate layer between SiC and Hastelloy X because its CTE lies between SiC and Hastelloy X. Also, it is a silicon-based ceramic which should have good corrosion resistance against boiling sulfuric acid. But it is highly brittle and requires a protective coating which SiC will act as.

References

1. Baykara, S.Z.J.I.J.o.H.E., *Hydrogen: a brief overview on its sources, production and environmental impact.* 2018. **43**(23): p. 10605-10614.
2. Vitart, X., et al., *Hydrogen production using the sulfur–iodine cycle coupled to a VHTR: an overview*. 2006. **47**(17): p. 2740-2747.
3. Dincer, I. and C. Zamfirescu, *Chapter 4 - Hydrogen Production by Thermal Energy*, in *Sustainable Hydrogen Production*, I. Dincer and C. Zamfirescu, Editors. 2016, Elsevier. p. 163-308.
4. Abanades, S., et al., *Screening of water-splitting thermochemical cycles potentially attractive for hydrogen production by concentrated solar energy.* 2006. **31**(14): p. 2805-2822.
5. Corgnale, C., M.B. Gorensek, and W.A.J.P. Summers, *Review of Sulfuric Acid Decomposition Processes for Sulfur-Based Thermochemical Hydrogen Production Cycles.* 2020. **8**(11): p. 1383.
6. Corgnale, C., Z. Ma, and S.J.I.J.o.H.E. Shimpalee, *Modeling of a direct solar receiver reactor for decomposition of sulfuric acid in thermochemical hydrogen production cycles.* 2019. **44**(50): p. 27237-27247.
7. Norman, J., et al., *Studies of the sulfur-iodine thermochemical water-splitting cycle.* 1982. **7**(7): p. 545-556.
8. Satpute, S.R., J.K. Park, and S.T.J.A.C.E.R. Revankar, *Effects of Excess Iodine and Water on Bunsen Reaction for Over-Azeotropic Limit.* 2015. **4**: p. 1-14.
9. Veziroglu, T.N. and F. Barbir, *Hydrogen energy technologies*. 1998: UNIDO.
10. Baykara, S.Z., *Hydrogen: A brief overview on its sources, production and environmental impact.* International Journal of Hydrogen Energy, 2018. **43**(23): p. 10605-10614.
11. Sivagurunathan, P., et al., *A critical review on issues and overcoming strategies for the enhancement of dark fermentative hydrogen production in continuous systems.* 2016. **41**(6): p. 3820-3836.
12. Das, D. and T.N.J.I.j.o.h.e. Veziroğlu, *Hydrogen production by biological processes: a survey of literature.* 2001. **26**(1): p. 13-28.
13. Zhang, Z., et al., *Photo-bioreactor structure and light-heat-mass transfer properties in photo-fermentative bio-hydrogen production system: A mini review.* 2017. **42**(17): p. 12143-12152.
14. Das, D. and T.N.J.I.j.o.h.e. Veziroglu, *Advances in biological hydrogen production processes.* 2008. **33**(21): p. 6046-6057.
15. Sattler, C., et al., *Solar hydrogen production via sulphur based thermochemical water-splitting.* Solar Energy, 2017. **156**: p. 30-47.
16. Sattler, C., et al., *Solar hydrogen production via sulphur based thermochemical water-splitting.* 2017. **156**: p. 30-47.
17. Bicer, Y. and I.J.I.J.o.H.E. Dincer, *Life cycle assessment of nuclear-based hydrogen and ammonia production options: A comparative evaluation.* 2017. **42**(33): p. 21559-21570.
18. Ni, M., et al., *A review and recent developments in photocatalytic water-splitting using TiO2 for hydrogen production.* 2007. **11**(3): p. 401-425.
19. Acar, C. and I.J.I.J.o.H.E. Dincer, *A review and evaluation of photoelectrode coating materials and methods for photoelectrochemical hydrogen production.* 2016. **41**(19): p. 7950-7959.
20. Liu, B. and Z.J.J.o.P.S. Li, *A review: hydrogen generation from borohydride hydrolysis reaction.* 2009. **187**(2): p. 527-534.

21. Kubo, S., et al., *Corrosion resistance of structural materials in high-temperature aqueous sulfuric acids in thermochemical water-splitting iodine–sulfur process.* 2013. **38**(16): p. 6577-6585.
22. Ginosar, D.M., et al., *Stability of supported platinum sulfuric acid decomposition catalysts for use in thermochemical water splitting cycles.* 2007. **32**(4): p. 482-488.
23. Vitart, X., A. Le Duigou, and P. Carles, *Hydrogen production using the sulfur–iodine cycle coupled to a VHTR: An overview.* Energy Conversion and Management, 2006. **47**(17): p. 2740-2747.
24. Corgnale, C., Z. Ma, and S. Shimpalee, *Modeling of a direct solar receiver reactor for decomposition of sulfuric acid in thermochemical hydrogen production cycles.* International Journal of Hydrogen Energy, 2019. **44**(50): p. 27237-27247.
25. Wong, B. and P.J.M.f.t.H.E. Trester, *Materials development for sulfur-iodine thermochemical hydrogen production*. 2008, CRC Press: Boca Raton. p. 81.
26. Dinovitzer, M., *Development and Characterization of Additive Manufacturing of Superalloy Hastealloy X Using a Cost Effective TIG Technique*. 2020, Carleton University.
27. Kazantseva, N.V., N.N. Stepanova, and M.B. Rigmant, *Superalloys: Analysis and Control of Failure Process*. 2018: CRC Press.
28. Samal, S.J.H.t.c., *High-temperature oxidation of metals.* 2016. **12**: p. 11-17.
29. Zhao, J.-C., et al., *Phase precipitation and time–temperature-transformation diagram of Hastelloy X.* 2000. **293**(1-2): p. 112-119.
30. Shen, C., et al., *The influence of post-production heat treatment on the multi-directional properties of nickel-aluminum bronze alloy fabricated using wire-arc additive manufacturing process.* 2018. **23**: p. 411-421.
31. Teeter, L., et al., *Comparison of the corrosion of materials in supercritical carbon dioxide, air, and argon environments.* 2021. **192**: p. 109752.
32. Petrovic, J.J., *Mechanical behavior of MoSi2 and MoSi2 composites.* Materials Science and Engineering: A, 1995. **192-193**: p. 31-37.
33. Afzal, W., et al., *Magneto-transport and electronic structures in MoSi2 bulks and thin films with different orientations.* Journal of Alloys and Compounds, 2021. **858**: p. 157670.
34. Hirvonen, J.P., et al., *Tribological characteristics of MoSi2/SiC nanocomposites.* Nanostructured Materials, 1995. **6**(5): p. 881-884.
35. Fu, Q.-G., et al., *B2O3 modified SiC–MoSi2 oxidation resistant coating for carbon/carbon composites by a two-step pack cementation.* Corrosion Science, 2009. **51**(10): p. 2450-2454.
36. Samadzadeh, M., et al., *Comparative studies of the oxidation of MoSi2 based materials: Low-temperature oxidation (300–900°C).* International Journal of Refractory Metals and Hard Materials, 2017. **66**: p. 11-20.
37. Gou, L., et al., *SiC film deposition by DC magnetron sputtering.* 1999. **345**(1): p. 42-44.
38. Loto, R.T. and P.J.C.E. Babalola, *Analysis of SiC grain size variation and NaCl concentration on the corrosion susceptibility of AA1070 aluminium matrix composites.* 2018. **5**(1): p. 1473002.
39. Ma, N.-n., et al., *Fabrication of amorphous silica coating on graphite substrate by laser cladding.* 2020. **46**(8): p. 10829-10834.
40. ke Chen, Z., et al., *Effect of microstructure on impact resistance of chemical vapor deposited SiC coating on graphite substrate.* 2019. **380**: p. 125076.

41. Li, S., et al. *Preparation of Molybdenum Coating on Surface of SiC Particles by Sol-Gel Method*. in *Advanced Materials Research*. 2013. Trans Tech Publ.
42. He, Z., et al., *Excluding molten fluoride salt from nuclear graphite by SiC/glassy carbon composite coating.* 2019. **51**(5): p. 1390-1397.

Chapter 3

Processing and Characterization Techniques

3.1 Physical Vapor Deposition (PVD)

3.1.1 Electron Beam Evaporation

Electron beam evaporations is a method in which the material to be deposited is bombarded with a high energy beam of electrons which evaporates the material. These evaporated molecules then reach the substrate and condense to form a layer on the surface of the substrate. The beam of electrons is generated using a heat filament and it is accelerated using an accelerator. On average if 1A of current is delivered to a 10kV system for creating emission acceleration, a power of 10kW will reach the surface of the material. To protect the filament, it is placed outside the zone of the evaporant as shown in Figure 3-1. A magnetic field B is utilized to bend the direction of the electron beam for protecting the filament.

The material to be deposited is evaporated in a water-cooled hearth, while the wafer, which is to be coated, is depicted as the substrate. As shown in the figure in terms of a resister, the heated filament produces the high intensity beam of electrons. A high vacuum is created before the start of evaporation process because it allows the evaporant molecules to roam freely inside the vacuum chamber. The evaporated molecules are then deposited everywhere including the substrate.

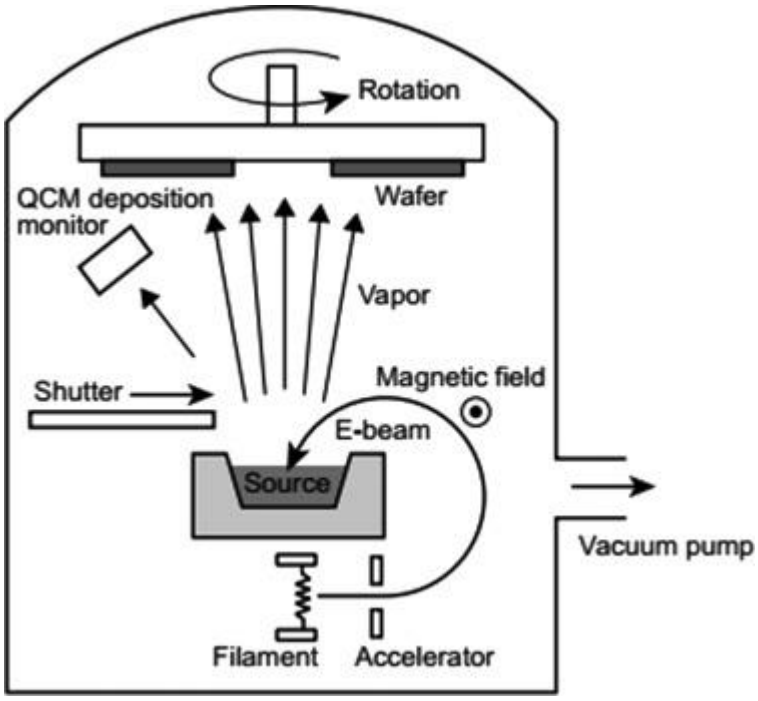

Figure 3-1 Electron Beam Evaporation system schematics [1].

Due to presence of electric and magnetic field inside the vacuum chamber, a combined force known as the Lorentz force is observed on electron of the beam. This combined force is given by Eq. 3-1.

$$F_c = \mathrm{F_e} + \mathrm{F_B} = \mathrm{q_e E} + \mathrm{q_e}(\mathrm{v} \times \mathrm{B}) \qquad \text{Eq. 3-1}$$

In this equation, F_c is the combined force in newtons, F_e and F_B are electric force and magnetic force. B is the magnetic field in Tesla, v is the velocity of moving electrons in ms^{-1}, q_e is the charge in coulombs and E is the electric field in Vm^{-1}. F_B is the cross product having direction perpendicular to both v and B as shown in Figure 3-1. F_e and F_B in Eq. 3-1 accelerates the electrons and deflect the electrons away from the filament. This curve is produced by F_B which is balanced by centrifugal force.

The operating principle is straightforward, and it is divided into three steps. The first stage involves heating the hot filament. The heated filament will generate an electron beam that is excited as a result of the heating. This can be accomplished by the use of thermionic emission. Thermionic emission is the discharge of electrons from a heated substance, in this case, a hot filament. The heated filament must provide enough energy for the electrons to overcome the attractive force that holds them

together for them to be excited. When electrons are energized and released, they can travel about at random.

The second stage is the heating of the deposition material. The to be deposited is placed inside a water-cooled hearth. The beam of electrons created by step one is the source of the heating process. Now, returning to stage one, because electrons are necessary to be employed as the source of boiling of the material in stage two, the electron beam must follow a specific path to be properly utilized. Excited electrons can move randomly in a high vacuum area without being attracted to it. As a result, magnets must be utilized to make it travel just towards the material to be evaporated. Two magnets are necessary for this situation. The first magnet, known as a focusing magnet, is used to attract charged electrons. A deflecting magnet will then be used to direct the electron beam's course towards the substance to be vaporized. The route towards the material has been constructed after the complete process of attracting and deflecting magnets, and the substance may now be heated. The material will be heated to a boiling point, which is defined by the evaporation principle; once achieved, the molecules in the liquid (material evaporant) will collide and transfer energy to one another, causing the liquid to convert into a vapor. As a result, the material evaporant may now travel freely in the high vacuum region.

When the material evaporant is able to move, it may migrate towards the substrate and link to it, which is the third and final step. As seen in Figure 3-1, the vapor may now move towards the wafer, enabling the material evaporant, which is now vapor, to condense over the whole surface of the wafer (substrate).

In a nutshell, electron beam evaporation is the process of employing an electron beam to evaporate (heat) material that will be used to deposit itself on a wafer (substrate). Electrons are created as a consequence of a heating process generated by a heated filament.

Electron beam evaporation is a type of physical vapor deposition used in fabrication and processing technology. It has its distinct method of depositing material on the wafer and hence has its own set of advantages and disadvantages in its application. It is typically used to make metalized wafers.

3.1.2 Sputtering

Sputtering is the process by which particles are ejected from a solid target material as a result of energetic particles bombardment. The bombardment of energetic particles heats the target surface and imparts velocity to the target particles, driving them to depart the surface. Typically, the energetic particles intended for bombardment take the form of ions. The vaporization of the target substance occurs because of ion bombardment. As a result, sputtering is regarded as a type of physical vapor deposition (PVD). Typically, the energetic particles bombarding the target are ions from a sputtering gas. These ions are generated primarily as a result of electron collisions with gas atoms as they travel from cathode to anode through the gaseous medium. Sputtering is a critical process. Sputtering is a well-established technique for controlling thin film deposition. Apart from thin film deposition, the technology is now extensively employed for surface cleaning and etching, as well as surface analysis and sputtering ion sources. There are various sputtering technologies available for the deposition of thin films.

3.1.2.1 Magnetron Sputtering

As electrons flow over the gaseous medium, which is responsible for developing and maintaining plasma, the majority of electrons must be collected prior to reaching the anode. Numerous design measures are taken to maintain the electrons in the gaseous medium for as long as feasible. The magnetron concept can be used to avoid rapid electron loss from the discharge. It is the most often used technique for thin film deposition. The magnetron is a cross-field device, as both the magnetic and electric fields are generated perpendicular to one another. By introducing an external magnetic field during the glow discharge, one can trap the electrons for longer periods of time, resulting in the generation of more positive ions at the same electron density. By encouraging electrons to take a curved path, the external magnetic field lengthens the electron flight. Electron collisions with unionized gaseous atoms/molecules are more likely on elongated paths. Increased collisions increase the possibility of ionization of the gaseous medium into positive ions and negative electrons. As a result, the cathode sheath and discharge pressure can be reduced. Now, the ions can reach the cathode with nearly full discharge potential, and the sputtered particles can reach the substrate surface with the fewest possible collisions. Additionally, this increases the deposition rate compared to a basic diode discharge device.

There are several methods for powering the target, ranging from direct current (DC) power for conductive targets to radio frequency (RF) power for nonconductive targets, as well as a variety of methods for providing voltage and/or current pulses to the target.

Direct current magnetron sputtering cannot be used to deposit insulating or semiconducting targets because the current cannot pass through non-conducting materials. As a result, radio frequency magnetron sputtering was created to produce insulating materials in order to alleviate this problem by introducing alternating current at a high frequency. Using this method, we can also deposit metallic compounds.

To ensure that the bulk of current is immersed in plasma, this deposition approach requires an impedance mating network. To convert current to high frequency, an RF source generator is required in addition to this matching network. As a result, RF magnetron sputtering equipment has a high manufacturing cost. The SiC coating was coated utilizing RF Magnetron Sputtering in the second portion of the study.

A glow discharge occurs when an electric current is passed through a low-pressure gas, resulting in the creation of plasma. Between the two electrodes, a potential difference is applied. When the applied potential exceeds the striking voltage (usually in the kV range), the gas ionizes and turns into a plasma, which begins conducting electricity and glows. The discharge characteristics are largely determined by the geometry of the cathode, anode, and vacuum vessel, as well as the electrode materials and gaseous medium used.

The electric field between the electrodes defines the electron paths in a simple diode glow discharge system. Electrons are accelerated when they pass through the cathode sheath and make a beeline for the anode electrode. A discharge can only be sustained if the electrons generate enough ions on their trip to the anode. Maintaining a sufficiently high pressure in the sputtering chamber is one way to assure a sustained discharge. However, the magnetron-assisted glow discharge system uses a magnetron source to prolong the electron's stay in the gaseous environment, resulting in the highest number of collisions and hence a sustained discharge.

Sputtering of a target material in the presence of a reactive gas or mixture of gases and a magnetron arrangement is referred to as reactive-RF magnetron sputtering. Sputtering is a technique that involves the sputtering of a target material in the presence of a reactive gas or a combination of gases. The coating's composition is determined by the sputtering atmosphere's composition. In other words, the reactive gas's kind and magnitude can be used to control the nature and chemistry of the sputtering material. Thus, by simply altering the chemistry of the sputtering atmosphere, a range of materials can be deposited from a single target. Argon (Ar) is typically used as the primary sputtering gas, however, the amount of reactive gas allowed into the process chamber dictates the stoichiometry of the coating to be formed in the majority of cases.

The reactive gas reacts with the materials with which it comes into contact. Inert gases such as nitrogen (N_2) become reactive during the sputtering process when violent collisions break them into atomic nitrogen (N) and charged species such as N^{2+}, N^{+}, and N^{-}. Additionally, reactive gases such as oxygen (O_2), hydrogen (H_2), carbon dioxide (CO_2), methane (CH_4), and ethylene (C_2H_2) are available.

3.1.2.2 Sputtering and Thermal Evaporation System.

NANOVAK NVTS-400 system was used to deposit SiC on $MoSi_2$ coated Hastelloy X using RF magnetron sputtering. This system is one of the most complex and intelligently managed systems available, and it can be operated through a computer screen. On this machine, you can conduct three separate operations:

- DC Magnetron Sputtering (with DC power capacity of 1560 W)
- RF Magnetron Sputtering (300 W capacity)

A stainless-steel chamber is coupled to a rotary pump and a turbo molecular pump as part of this system. In 3 hours, a vacuum of 5 x 10^{-8} torr can be created. It comes with two vacuum gauges: a highly precise magnetron Pirani vacuum gauge for measuring vacuum from atmospheric pressure to 10^{-9} torr and a capacitance diaphragm gauge for measuring working gas pressure. With a sample rotation speed of 5 to 30 rpm, a substrate temperature of 500 degrees Celsius can be obtained. It also has thickness controllers that can measure thickness down to 0.1Å.

3.2 Dip Coating

Dip coating is a highly successful method for producing thin films. The solution substrate is immersed in the solution to ensure that the material is formed effectively. Once the material is deposited, the substrate can be removed via evaporation, resulting in a layer with a unique thickness. The dip-coating process is primarily driven by inertia, viscous drag, gravitational force, and surface tension. The advantages of dip coating are its inexpensive cost and the ease with which layer thickness can be altered. The disadvantages of dip coating are that the procedure is sluggish and that it has the potential to obstruct the screen, which will have a significant impact on the final result.

Dip coating is another solution-based wet chemistry method for the deposition of films with thickness from 25 nm to 60 μm allowing high precision in dip coating. To coat a substrate, a liquid coating material is immersed in a solution for a period and then extracted quickly. The coating process was carried out in a temperature-controlled environment. The coating's thickness can readily be adjusted. The solution's viscosity, withdrawal rate, and solid content all play a role. Thicker coatings and more viscous solutions result when substrates are withdrawn at a faster rate. The advantage of using dip coating is that it is cheap and simple. It allows us to control the film thickness. Dip tanks come in different variety of shapes and sizes which allows coating on large and small substrates. The film may be thicker at one edge of the substrate and thinner at the other.

Dip coating is accomplished by dipping a substrate in a precursor solution and then vertically raising it out of the solution at a velocity v_0. Along with the moving substrate, a wet film with thickness is drawn upward from the liquid. While it may appear to be a simple process at first glance, the dip-coating process is a complex interplay of numerous opposing forces, including gravity acting on wet film and the wet film's surface tension in the concavely shaped meniscus, surface tension gradient along with the film's height due to drying effects, disjoining (or conjoining) pressure, and others. The Landau and Levich relationship as given in Eq. 3-2 can be used to estimate the wet film thickness.

Eq. 3-2

$$\lambda = 0.94 \frac{(\eta v_0)^{2/3}}{\gamma_{LV}{}^{1/6} \sqrt{\rho g}}$$

Here, γ_{LV} denotes the liquid's surface tension at the meniscus point, and g is the standard gravity (9.81 m/s^2). The second method of dip coating is to keep the substrate horizontal while lowering it until one of the substrate faces makes contact with the liquid surface. Additionally, dip coating can be utilized to create irregular and complex shapes.

Multiple samples may be prepared in a single draw using a dip coater, which has a temperature-controlled chamber. A computerized controller with a touch screen is used to regulate the pulling and dipping speeds. Dip/pull rate, dwell duration within and outside the liquid may be configured to cover six samples automatically.

Figure 3-2 Dip Coater (WPTL6-0.01 by MTI).

Precision-controlled pulling and dipping rates from 1 mm/min to 40 mm/min. The temperature chamber can be heated up to 100℃ with ±1℃ accuracy. The dip coater used in this research is shown in Figure 3-2.

3.3 Characterization

3.3.1 Scanning Electron Microscopy

Scanning electron microscopy (SEM) works on the principal or interaction of highly energetic electrons in the form of a focused beam, and a sample surface. This incident of electron beam creates multiple signals to create an image on the sample. The reflected samples can give knowledge about microstructure, materials orientation, morphology, topography, and composition of the sample under observation.

Figure 3-3 TECASN Vega 3 Scanning electron microscopy.

A scanning electron microscope as shown in Figure 3-3 typically requires an electron gun to eject electrons. The electron gun typically employs a tungsten filament, which upon heating thermionic ally emits electrons. These electrons are accelerated towards the anode by a high electric field. A portion of the electrons, due to high velocities pass by the anode plate and stream down the column. In the process, the electrons acquire energy typically in the range of 0.2 – 40 keV. The electrons are then focused by one or two lenses to a spot of diameter in the range of 0.4 to 5 nm. This is followed by the passages of the beam through a pair of scanning coils or deflector plates. Here the beam is deflected in the xy-plane to cause a raster scan of the sample. Selected areas, as well as selected points, could be analyzed with SEM. Fast and

energetic electrons interacting with the sample surface generate different types of signals that are detected by using specific detectors. Mainly two types of detector are used secondary electron and back scatter electron. SE is especially important for morphology imaging and topography. BSE is often employed for showing compositional.

3.3.2 Energy Dispersive X-ray Spectroscopy

Energy-dispersive X-ray spectroscopy (EDX) is a technique for determining the elemental composition of a sample. It is also known as energy dispersive X-ray microanalysis (EDXMA) or energy dispersive X-ray analysis (EDXA). EDS is based on the idea that every element is made up of atoms with a distinct atomic structure. As a result, each element can generate a distinct set of distinctive x-rays when excited. The bombardment of a material with a beam of highly charged particles (electrons or protons), or X-rays, is required to produce X-rays. As a result, EDS entails elemental analysis of the X-ray spectra acquired as a result of the bombardment. Electrons may be taken from a surface when particles/radiations fall on it, depending on the energy of the falling particles/radiations and the binding energies of the electrons. Particles/radiations with sufficient energy can even remove inner shell electrons from sample atoms. When an electron from the inner shell is removed, a vacancy (hole) in that shell is generated. That hole is filled by an electron from an outer orbit. This transition causes X-ray emission, which is a property of that element. A capital letter marks the shell where the vacancy existed on the X-ray lines. It might be K, L, or M, followed by a Greek letter (α, β). The most significant ones are the α lines. B lines are less important than α lines indicated by other Greek letters that follow but more important than lines indicated by other Greek letters that follow, and so on. The Greek letter is followed by a number (1, 2, etc.) in subscript, that corresponds to the intensity of the line in that peculiar group, such as $K\alpha_1$. Among the numbers, 1 stands for maximum intensity, while others in the sequence represent a correspondingly decreasing intensity. When there is no number mentioned, it represents the combined intensity from all the X-rays in that group, such as Kα. Sometimes, the combined line is represented by mentioning more than one number in the subscript, such as $K\alpha_{12}$. All elements with atomic numbers in the range 4–92 are detectable with EDS. EDS analysis may be qualitative or quantitative. Qualitative analysis is fairly simple since it involves lines identification in the X-ray spectrum. Quantitative analysis is relatively

complicated because it involves not only line identification but also intensity measurement of each element in the sample as well as of the same elements in calibration standards of known composition. The precision of the quantitative EDS is primarily limited by statistics since EDS involves photon counting for intensity measurements. For most of the elements, a relative precision of better than ±1% is achievable. However, due to limitations introduced by the standard compositions as well as a set of corrections, the analytical accuracy of EDS is near ±2%. For EDS analysis samples must also be conductive. For the insulator, a thin layer of gold or carbon is deposited to avoid charging for the sample. In this study, an Oxford EDS detector attached with TESCAN VEGA 3 SEM was used.

3.3.3 Cross-Sectional SEM Analysis

It is one of the most important methods for studying the thin film-substrate interaction. This tool can also be used to figure out how thick a thin film is. Sample preparation is a necessary skill for cross-sectional analysis. The results can only be informative if the sample has been properly prepared and has gone through all of the essential sample preparation steps. Careful cutting, grinding, and polishing are frequently required. The samples were ground and polished on a Metkon FORCIPOL grinding and polishing equipment.

Cleaning the sample is a crucial step. Sample preparation methods were adjusted in this study to achieve the appropriate configuration for cross-sectional analysis. The steps for preparing a sample are as follows.

- At first, the coated sample is cut down to the desired size
- Suitable mold is selected
- Epoxy is prepared by mixing it with a hardener in a suitable ratio
- The sample is then embedded in the epoxy
- After settling of the sample, grinding and polishing is done with suitable grit size paper
- The sample is then cleaned and stored
- For SEM analysis, the sample is coated with gold up to a few nanometers
- SEM imaging and processing is done at the end

In addition to it, the resolving power of SEM is considerably higher than an optical microscope. SEM uses electrons of energies as high as thousands of eV. It can resolve images up to 1nm. In this work, film morphology and cross-sectional analysis were done by using TECASN Vega 3 SEM.

3.3.4 X-ray Diffraction

The electron in an atom scatters light coherently, therefore each atom in the crystal functions as a coherent scattering point. The light scattering strength of an atom is determined by the number of electrons in that atom. Crystals can diffract X-rays because they are made up of a periodic array of long-range organized atoms. The X-rays scattered by atoms in a substance carry information about the material's atomic organization. Because less crystalline or amorphous materials lack periodic structures, x-ray diffraction does not reveal a distinct pattern. A varied pattern is expected for different atom arrangements. Multiple peaks can be seen in a single diffraction pattern of the material.

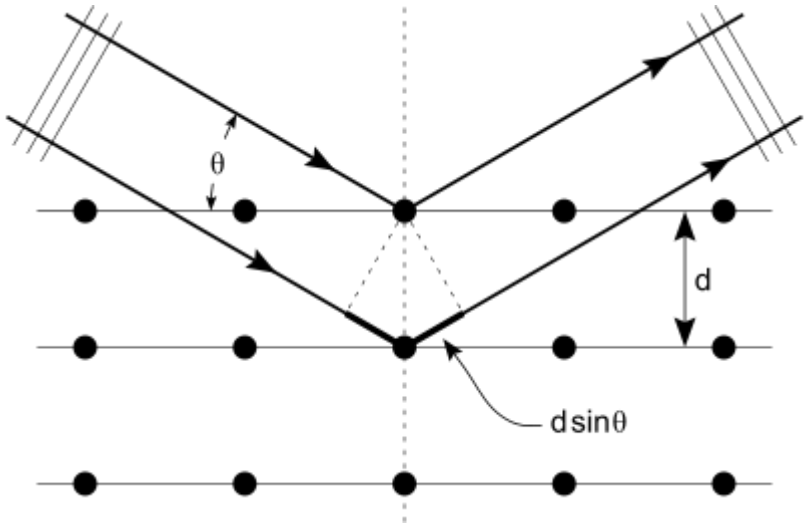

Figure 3-4 Bragg's law.

The number of peaks and their relative intensity are determined by the material's crystal structure. The structure of a crystal is defined by its unit cell, whereas the shape of the unit cell is described by a crystal system. Different planes of atoms are identified by Miller indices (hkl).

X-ray diffraction wavelength λ falling on a family of parallel atomic planes, constructive interference occurs only at a specific angle as shown in Figure 3-4. Bragg's formula is given in Eq. 3-3.

$$n\lambda = 2d \sin\theta \quad \text{Eq. 3-3}$$

Where, n is a positive integer, which indicates the inter-planar distance between two adjacent planes of the (hkl) family. Furthermore, inter-planar spacing (d) using Eq. 3-4 and lattice parameter was calculated by Bragg's formula given in Eq.3-4.

$$\frac{1}{d^2} = \frac{h^2 + l^2 + k^2}{a^2} \quad \text{Eq. 3-4}$$

The crystallite size is calculated using full-width half maxima of the characteristic XRD peaks using the Scherer formula as given in Eq. 3-5.

$$D_s = \frac{0.9\lambda}{\beta \cos\theta} \quad \text{Eq. 3-5}$$

D_S is crystallite size, where, λ shows the wavelength of the X-Ray which has a constant value of 1.54, θ is Bragg diffraction angle, β represents full width at half-maximum (FWHM) in radians.

3.3.5 Fourier Transform Infrared Spectroscopy (FTIR)

FTIR spectroscopy involves chemical bonds and functional groups identification because of IR absorption by a specimen. These absorptions can be associated with the stretching and bending of covalent bonds of molecules of a specimen. Stretching vibrations, which are further classified as symmetric and asymmetric vibrations, are typically high energy vibrations than bending vibrations. The results of IR spectroscopy are typically plotted as IR transmittance or absorbance vs IR frequency. Frequencies are represented as wavenumbers in units of cm^{-1}. The typical frequency range for IR spectroscopy is from 400 cm^{-1} to 4000 cm^{-1}. The intensity of the bands due to absorption in the transmittance or reflectance spectra depends on the dipole moment of the polar bond. For strong polar bonds, strong IR bands are observed.

IR spectroscopy is useful for identifying molecular fragments such as functional groups, thus providing information on the molecular fingerprint of materials. IR spectroscopy, however, does not provide proof of chemical formula or structure.

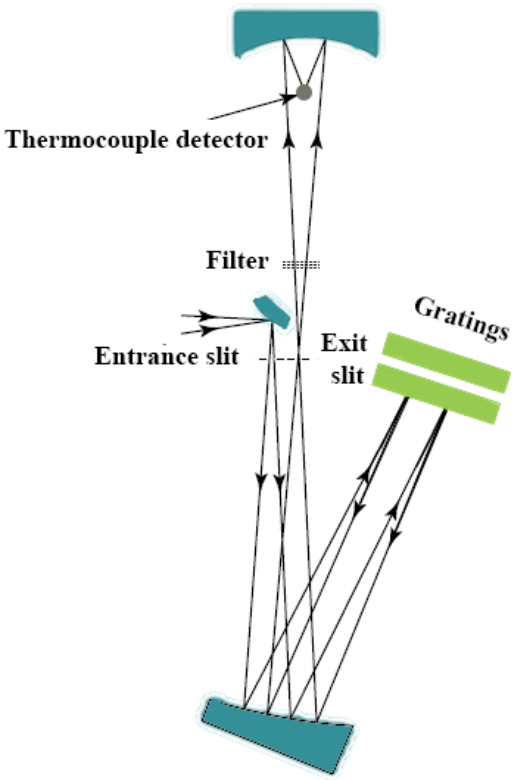

Figure 3-5 A basic double beam dispersive IR spectrometer with gratings.

Dispersive instruments have been traditionally applied for obtaining IR spectra. Prisms were used in the first dispersive IR instruments. Later on, gratings replaced the prisms in these devices. A monochromator contains the prism/grating. As shown in Figure 3-5, the dispersive element disperses the energy entering through the entrance slit and reflects it towards the exit slit. At the exit slit, the spectrum is scanned before passing it forward to meet the detector. Typically, the slit size of both the entrance and exit slits is programmed to vary to compensate for any variation of the input (source) energy with frequency. Thus, upon scanning the spectrum, the detector receives almost constant energy, provided no analysis sample is inserted.

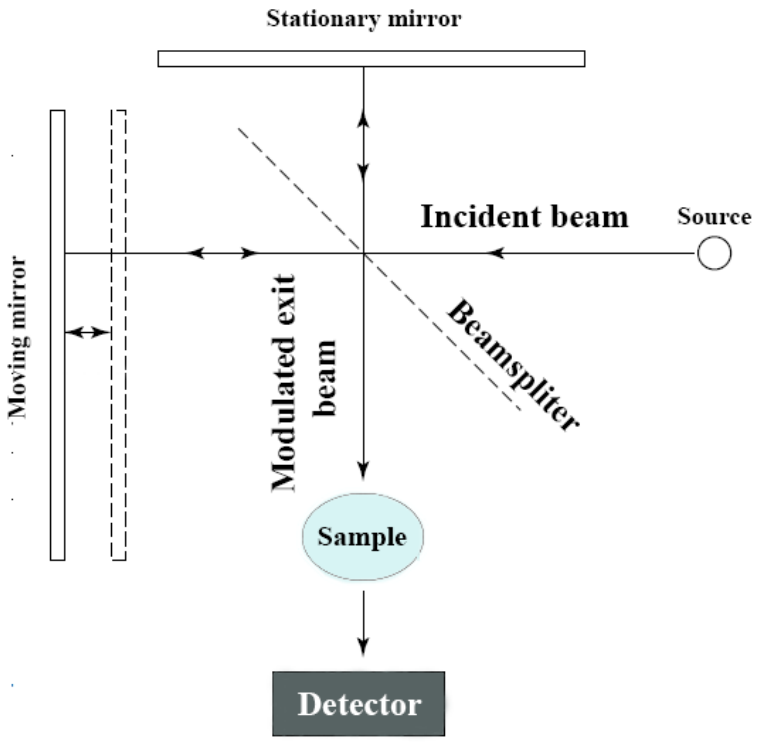

Figure 3-6 Schematic of a basic Michelson interferometer.

During the 1970s, commercial IR instruments employing a very different method were introduced. These instruments quickly replaced the traditional dispersive instruments. Spectrometers today predominantly employ the Fourier transform method to obtain the IR spectra, hence the name Fourier transform infrared (FTIR) spectrometers. These devices are superior in performance as well as data handling capability. An FTIR instrument employs an amplitude division interferometer such as the Michelson interferometer for its operation. As shown in Figure 3-6, an interferometer involves splitting a beam into two and directing each of these along different paths to reflecting mirrors. The mirrors reflect these back and recombine them into one single beam.

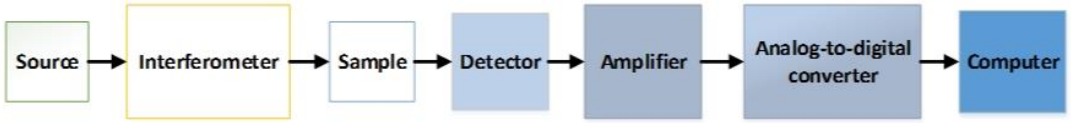

Figure 3-7 Basic block diagram of an FTIR spectrometer.

The position of one of the mirrors is mechanically scanned, to result in a difference in path length for the two split beams. Thus, an interferogram of a time-

dependent intensity of the transmitted energy can be obtained. For monochromatic IR illumination on the interferogram, an interferogram with a sine wave should be obtained. However, if the interferometer gets illuminated by a broad polychromatic IR spectrum, the interferogram would correspond to an interference pattern on an infinite number of sine waves of different wavelengths and periods. Figure 3-7 elaborates the basic block diagram of FTIR.

Literally, any sample in any state may be analyzed with FTIR spectroscopy. Gases, liquids, pastes, powders, solutions, films, fibers, and surfaces are all examinable with FTIR, provided a judicious sample preparation choice is made. Mix the sample with a mulling agent (mineral oil etc.) and press between NaCl plates. NaCl is used because it is cheap and is capable of avoiding IR absorptions up to the 650 cm^{-1} mark. However, below 650 cm^{-1}, NaCl plates become absorbing as well. On the other hand, KBr plates, which are costlier than NaCl, remain transparent to 400 cm^{-1} point. Although the salt may be IR transparent, the mineral oil used is an IR absorber, and that's the downside of this technique.

The second technique is the KBr method, which involves mixing the sample with KBr and making pellets of the mixture through high-pressure pressing. The mulling agent and hence the absorptions associated with the mulling agent are avoided in this case. Only solids could be analyzed with this technique and that's the limitation of this method.

3.3.6 Atomic Force Microscopy (AFM)

Atomic force microscopy (AFM) as shown in Figure 3-8 is a surface examination technique that creates three-dimensional photographs of a surface in order to study nanometric and sub-nanometric details. This approach works with any sort of material, regardless of its hardness, transparency, or conductivity. AFM is made up of a sample holding, a probe attached to a cantilever, and measuring hardware controlled and monitored by a computer program. The cantilever can be thought of as a spring, and the force experienced by the probe is determined by the spring constant and the distance between the probe and the surface. Eq. 3-6 gives the force according to Hook's law.

$$F = -kx \qquad \text{Eq. 3-6}$$

When the value of the spring constant and K (0.1 – 1 N/m) is smaller than that of the surface, a cantilever bending occurs. The normal range of this force in the air is 10^{-6} N–10^{-9} nN. The probe motion over the surface is controlled by feedback networks and piezo electronic scanners. The fundamental driver behind today's instrumentation systems is to monitor the force between the probe and the surface. The deflection of the probe is measured using light reflection phenomena. The beam bounce method is the name for this technique. The bending of the cantilever was measured by the detector, which was then mapped by the computer in advance to form a 3D image on the surface.

Figure 3-8 FLEX Atomic Force Microscopy

The contact and non-contact modes of operation are the two basic modes of operation. The probe's major interactions in the contact mode of operation are repulsive Van der Waals forces. In non-contact mode, however, the probe is relatively far away from the surface, and attractive Vander Waals interactions are most important. A probe is used to measure heights. When the probe is brought close enough to the sample surface, it generates a number of forces, which may be used to calculate the height. FLEX AFM was used to get topographic pictures of $MoSi_2$ coated Hastelloy X samples in this investigation. To assess the relationship between the roughness of the surface and the relevant deposition characteristics of the samples, the roughness of the surface was measured and compared.

Summary

Physical vapor deposition techniques were employed in multiple experiments along with the wet chemistry method through dip coating. Among the physical vapor deposition, electron beam evaporation and radio frequency magnetron sputtering were discussed in detail while focusing on the underlying principle of operation. Dip coating is another wet chemistry low-cost deposition technique.

Several characterization approaches were used to describe thin films. The working principle of X-ray diffraction has been discussed. The principles regulating scanning electron microscopy and energy-dispersive X-ray spectroscopy have been explored. The fundamental principles of infrared spectroscopy have been discussed, as well as a comparison of classical dispersive IR spectroscopy and Fourier transform infrared spectroscopy. The operating principle of atomic force microscopy, as well as its various modes of operation, have been thoroughly explored in this section.

References

1. Bashir, A., et al., *Chapter 3 - Interfaces and surfaces*, in *Chemistry of Nanomaterials*, T.I. Awan, A. Bashir, and A. Tehseen, Editors. 2020, Elsevier. p. 51-87.

Chapter 4

Experimental Methods

4.1 $MoSi_2$ layer via Electron Beam Physical Vapor Deposition

4.1.1 Sample Preparation of Hastelloy X

Hastelloy X was cut into desired sizes by using a low-speed diamond cutter off the MTI group (SYJ 150 model). The diamond blade was used to cut Hastelloy X. the speed was set at 100 rpm for 2x2 cm samples. Meanwhile, for 1x2 cm the speed was set to 50 rpm. The coolant used was distilled water. The substrates were cleaned with acetone and air-dried in the oven after cleaning. The substrates were polished up to 3 microns from both sides.

The model used is certified equipment called SYJ-150 low-speed diamond saw. It is equipped with an advanced digital micrometer and digital display. The machine can cut/slice/dice a material up to 32.5 mm. Three blades are used for operating this machine. These are

- Diamond Blade
- SiC or Ceramic Blade
- Alumina Blade

The diamond blade is used to cut materials like plastic, crystals, and ceramics. Meanwhile, SiC blades are used for superalloys and non-ferrous metals. Lastly, an Alumina blade is used for cutting steel and ferrous metals. The parameters set for this experiment are given in Table 4-1.

Table 4-1 Parameters for Low-Speed Diamond Saw Cutter.

Parameters	Details
Speed	100 rpm Low speed because the material is hard and at high speed, the diamond blade will be damaged.
Coolant	Distilled Water The water level should always be more than 80 % to ensure the cooling of the blade.
Blade Type	Diamond SiC is preferred but diamond can also cut superalloy.
Substrate	Superalloy
Thickness of Substrate	1.5 mm

The substrate was cut into proper sizes in a low-speed diamond saw cutter machine. The make and model of the machine are SYJ-150 of the MTI company as shown in Figure 4-1. The instrument was first cleaned using oil. the blade used was made of the diamond by MTI company. The micrometer was adjusted inside the copper tube and tightened by a screw on the backside of the machine. The manipulator's arm was adjusted at such a position so that the blade will not cut into the machine. The angle at the manipulator's arm was adjusted at 90º. The bolt was adjusted such that the stopper switch will be activated once the sample is cut completely. It can also be used for protection against overcutting of the sample. The blade was placed between the clams onto the principal shaft. Distilled water was used as a coolant. It

was poured inside the tray which was placed under the blade. Some part of the blade was in contact with the coolant. The water splash guard was set up after that. The substrate was placed inside the mini wise and it was fixed tightly so that during cutting it will not change its position.

Figure 4-1 Low-Speed Diamond Saw Cutter.

The machine was started, and the blade moved freely in the coolant for about 1 minute. After that, the substrate placed inside the mini wise was slowly brought in contact with the blade through the working arm. The targeted size for the substrate was marked before using measurement tools. The position was adjusted using the micrometer so that the blade would cut on the exact cutting mark. The position of the blade was adjusted onto the mark on the substrate by using the micrometer.

The first cut was made at default speed. After that, the speed was adjusted to 100 rpm. At default speed, the blade stopped due to low rpm but when it was changed to higher rotational speed, the blade cut smoothly. The length of the total cut was 21.7 mm. This process was completed in four steps because after every 15 minutes, the machine was stopped to let it rest. A total of four cuts were made. Their details are given in Table 4-2.

Table 4-2. Experimental Details of Low-Speed Diamond Saw Cutter on SYJ-150 for cutting superalloy.

Cut	Total Time Taken	Dimension	Details
1	1 hour 20 min 25 sec	22.8 × 21.7 mm	~100rpm and Weight not attached on the back of the holder
2	1 hour 2 min 34 sec	21.3 × 21.8 mm	~100 rpm and Support weight not attached
3	24 min 14 sec	21.3 × 10.5 mm 21.3 × 11.3 mm	~100 rpm, support weight attached on the back
4	38 min 50 sec	10.01 × 10.5 mm	~100 rpm, support weight removed
5	50 min 15 sec	22.7 × 21.3 mm	~100 rpm support weight removed

4.1.2 The deposition process of $MoSi_2$ via EB PVD

The films were coated inside an NVEB-600 E-beam system as shown in Figure 4-2. Molybdenum disilicide charge was placed inside a molybdenum crucible to protect the system in case the charge melted. The sample was placed inside the sample holder and the base pressure was set to $1*10^{-6}$ torr using a turbomolecular pump. The substrates were heated to 200℃ and the voltage was set to 6kV. The current was varied between 30-70mA at the start but set to 60mA and the sample rotation speed was set to 10rpm. Films were deposited at the rate of about $1Ås^{-1}$. The final thickness of the film was 1 micron which was achieved in three sessions.

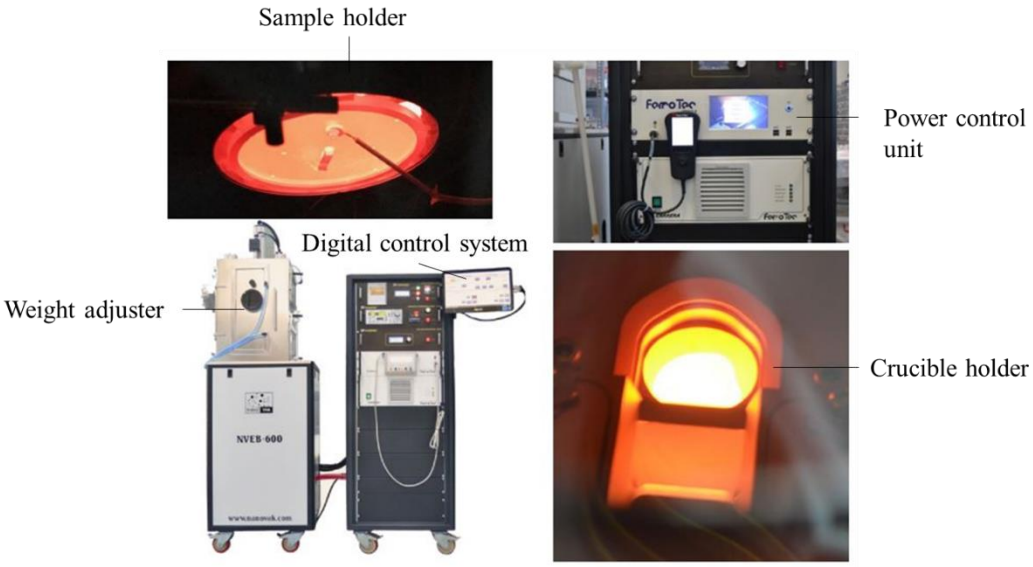

Figure 4-2 E-beam System NVEB 600.

The parameters set in this experiment are given in Table 4-3.

Table 4-3 E-Beam Deposition Parameters.

Substrate	**SS-304 and Hastelloy-X**
Charge material	$MoSi_2$
Voltage	6 kV
Current	60 mA
Base Pressure	2.3×10^{-6}
Deposition Rate	1.08 Å/s
Substrate Temperature	200℃

The substrates were first placed inside the sample holder. Clips were used to fix the sample so that it does not fall inside the chamber during deposition. Adhesive tape was not used to attach the sample because of substrate heating.

After the sample holder was placed inside the chamber, the charge of $MoSi_2$ was placed inside the charge holder. The quantity of $MoSi_2$ used was in such amount that the surface was leveled with the crucible in which the charge was placed. The crucible in which the charge was placed was made of molybdenum.

After placing both samples and charge inside the chamber, the machine was turned on and a vacuum was created inside the chamber. The pressure achieved inside the chamber was $2.3 * 10^{-6}$ torr. As the pressure was being achieved, we increased the substrate temperature to 200℃ gradually at 15℃ ramp each time. The heating was done slowly to maintain the vacuum because an increase in temperature causes an increase in pressure.

Once both the temperature and pressure were achieved, we turned on the High Voltage (HV) section of the machine. It means the voltage was supplied to the electron gun and the current was controlled by a manual controller. The voltage given was 6kV. On the HV module, there were four available slots present at one time for each charge placed. We selected the charge of $MoSi_2$ and the charging tray inside the chamber rotated to and our desired charge was in place.

The sweep frequency was set to 50 and 51 Hz for both Quartz Crystal Monitors (QCM) to measure the film thickness deposited onto the substrate. The flowsheet diagram of this process is shown in Figure 4-3.

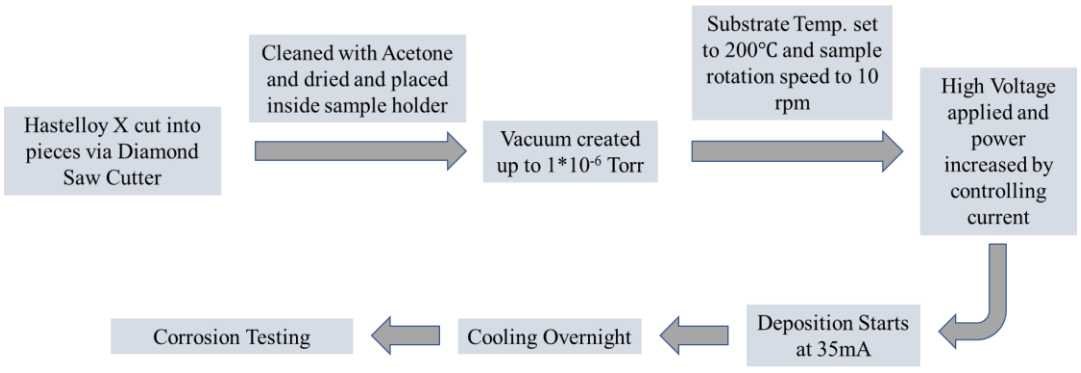

Figure 4-3 Flow Diagram of $MoSi_2$ Coating on Hastelloy X.

4.1.3 Characterization

The surface morphologies of $MoSi_2$ thin films were monitored with scanning electron microscopy. The impact of process parameters on cryptographic and

structural characteristics of molybdenum thin film on graphite was observed with X-Ray Diffraction using CuKα source. The XRD data was analyzed by MDI Jade 6.5 which shows us FWHM, d spacing, peak intensity, and different cryptographic features. Hall Effect was employed to demonstrate the trend of resistivity.

4.2 RF Magnetron Sputtered SiC on $MoSi_2$ coated Hastelloy-X

4.2.1 The deposition process of SiC on $MoSi_2$ coated Hastelloy X

Silicon carbide thin film was deposited on Hastelloy X by RF Magnetron Sputtering. NANOVAK NVTS 400 was used for this purpose. After sample placement, a high vacuum was built up to 5×10^{-7} torr by a Turbo-molecular pump. The deposition process is elaborated in flow sheet form in Figure 4-4.

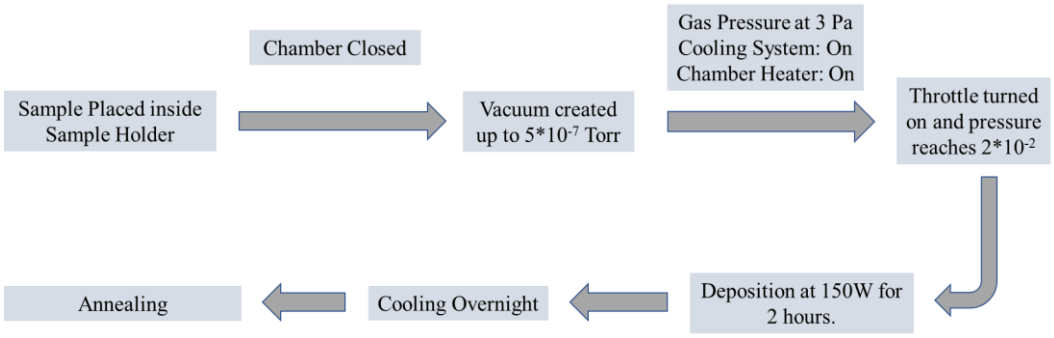

Figure 4-4 Flow Diagram of SiC Deposition via RF Magnetron Sputtering

The substrate temperature was increased up to 300°C. Moreover, substrate rotation speed was kept at 5 RPM. The gas pressure of 3 Pascal was used along with RF power of 150 W. 900 nm Silicon carbide thin film was deposited in 2 hours. The system is shown in Figure 4-5.

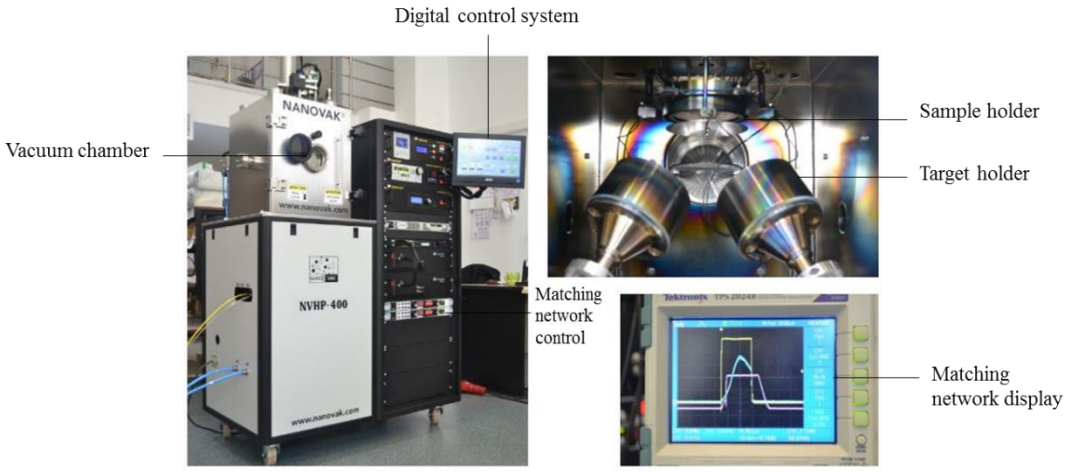

Figure 4-5 Sputtering System NVHP-400.

The substrates were first placed inside the sample holder. Clips were used to fix the sample so that it does not fall inside the chamber during deposition. Adhesive tape was not used to attach the sample because of substrate heating.

After the samples were placed inside the sample holder, the SiC disk of 99.99% purity was fixed inside one of the target holders. The placement of the target holder was staged in such a way as to maximize the deposition of SiC onto the samples. After that, the chamber was closed.

The vacuum was built up to 5×10^{-7} torr with the help of a turbomolecular pump. The initial power was set 10W and the final power to 100W initially. At 15W plasma was achieved but the deposition rate was much slower. To increase the deposition rate, power was increased gradually with the help of software installed in the tablet of the machine.

At high power, the issue of reflected power was dealt with with the help of tuning the matching network present inside the system. The thickness was measured by QCM already installed inside the system.

4.2.2 Heat Treatment

MTI GSL 1600 tube furnace was used for sintering and reactive annealing of various coated thin films. GSL-1600X-50-UL contains a 5 cm tube with silicon carbide-based heating rods. It can be used in annealing and sintering experiments at elevated temperatures. Under vacuum conditions, they can be increased up to 1600℃.

Temperature is controlled by an SCR controller with high precision of 1K. This tube furnace contains a high-quality tube with 99.99 % pure alumina. It also includes pressure gauges to monitor pressure inside the tube furnace. This tube furnace can be operated with different gases like nitrogen, argon, and helium. Annealing experiments can be performed in the air as well. This tube furnace is highly compatible with the glove box as well. Figure 4-6 shows the GSL-1600X-50-UL furnace.

Figure 4-6 MTI GSL 1600 tube furnace.

4.2.3 Characterization

TESAN VEGA3 scanning electron microscope was used to observe the surface morphology of silicon carbide thin film. Bruker D8 advanced X-rays diffractometer with CuKα as a radiation source was employed to determine the structural properties of the thin film.

4.3 SiC deposition via Dip Coating

4.3.1 Slurry Preparation

For slurry preparation polyethylene glycol (PEG) 0.8wt% was mixed in distilled water under magnetic stirring. After the PEG was completely dissolved, oxidized SiC powders were gradually added to the mixture. The slurry was prepared by adding oxidized SiC powders 66% vol. in distilled water and PEG mixture at room

temperature. After constant magnetic stirring, the slurry was sonicated for 30 minutes in an ultrasonic bath. The prepared slurry was aged for one day and then deposited onto the substrate.

4.3.2 Deposition

The as-prepared slurry was deposited onto Hastelloy X via dip-coating technique. the substrate was placed inside the dip coater such that the sample was 2mm away from the surface of the prepared slurry. The substrate was dipped inside the slurry for 30 seconds about 15mm to obtain a deposited area of around 1x1 cm accommodating for the distance between the substrate and the slurry. This completed one cycle. The flowsheet diagram of this process is given in Figure 4-7.

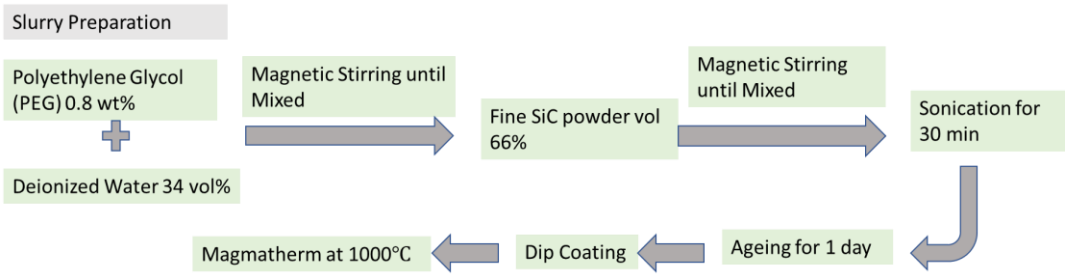

Figure 4-7 Flow Diagram of Dip Coating Process.

After three cycles, the as-coated sample was dried at 100℃ and then coated again. A thick-coated sample was obtained. Both the immersion and withdrawal speed was set to 35mm/min. After that, the sample was annealed at 1000℃ for 2 hours in the air inside a furnace with a ramp of 7℃/min.

4.3.3 Characterization

TESAN VEGA 3 scanning electron microscope was used to determine the surface morphology of the deposited film. FTIR was carried out in CARY 603 by Agilent Technologies to determine the SiC deposition.

4.4 Corrosion Testing

4.4.1 Low-temperature corrosion testing

Immersion tests were carried out in 98% sulfuric acid via the weight-loss method. The testing parameters were set as immersion in acid for 4 hours at 60℃ and

2 hours at 120℃. The experiment was performed inside an autoclave. 15mL sulfuric acid was poured into the Teflon inliner which was then placed inside the autoclave. The oven was preheated to desired temperatures and the sample was immersed inside the acid. The autoclave was placed inside the preheated oven and time was noted. When the experiment was completed, the autoclave was taken out from the oven and the sample was collected. The schematic diagram of the experiment is shown in Figure 4-8.

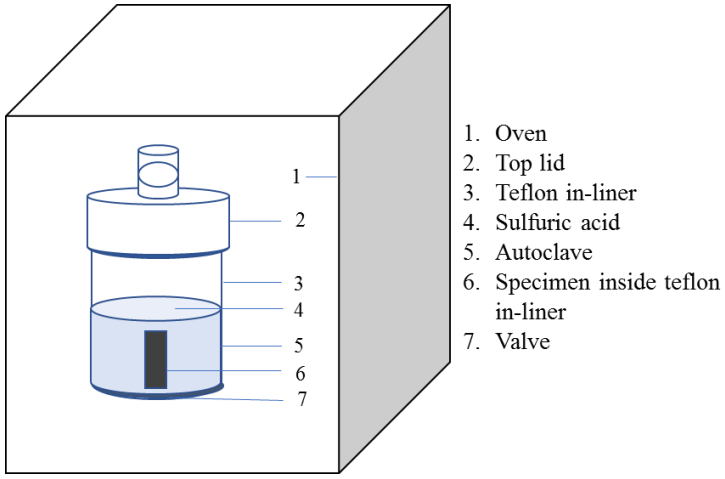

Figure 4-8 Immersion experiment apparatus in liquid phase sulfuric acid.

The sample then underwent a cleaning process. The process included cleaning with distilled water and then air-drying. The samples were weighed ten times before and after the experiment to address any random error.

4.4.2 High-temperature corrosion testing

Corrosion tests were carried out at a boiling temperature in 98% conc. sulfuric acid. The experiment was performed in the setup as shown in the figure below. A round bottom flask was covered in glass wool and then placed inside an electric heater with a max temperature of 500℃. The wires of the heater were connected with the PID (Proportional, Integrative, Derivative) controller. A thermocouple was attached with PID control in such a way that the tip of the thermocouple was in contact with the glass of the flask for accurate measurement of the temperature. The schematics of the system are shown in Figure 4-9.

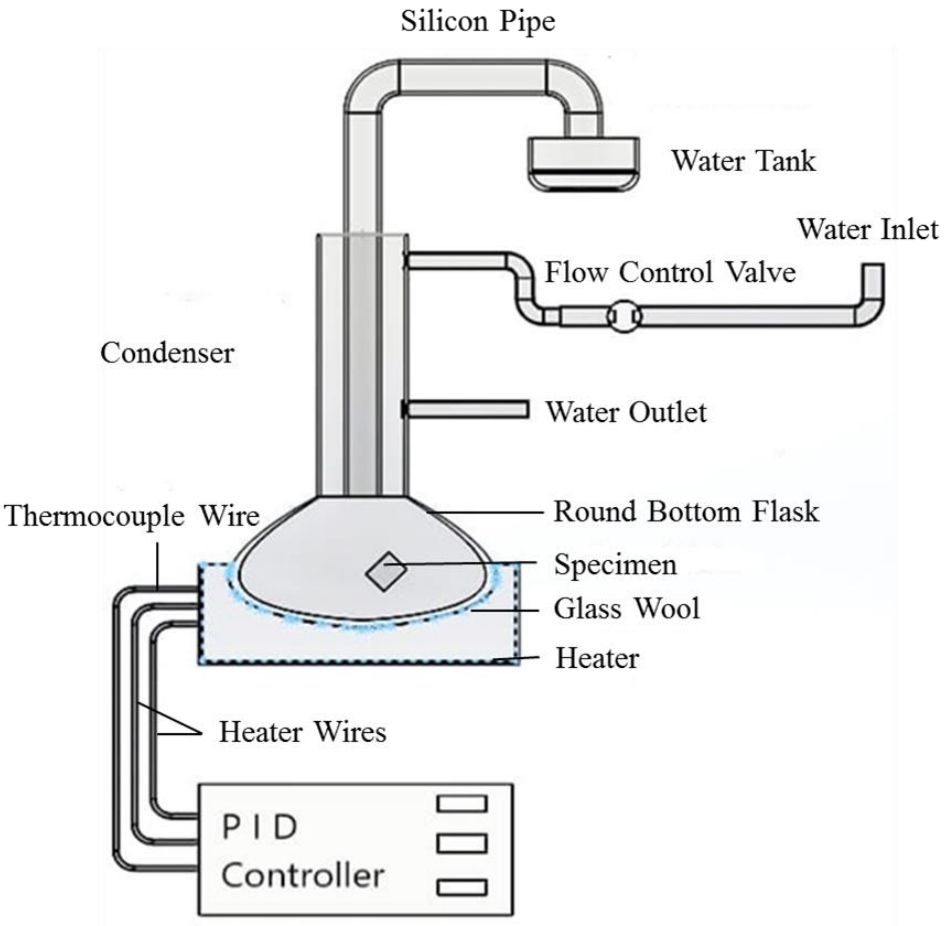

Figure 4-9 Schematic Diagram of corrosion testing at high temperature.

For cooling purposes, a condenser was used in such a way that the condenser was fixed inside the custom-made round bottom flask so that no fumes of acid be released in the environment at high temperatures. The inlet of the condenser was connected to a water pump and the outlet was connected to a pipe that removed the hot water from the system. At boiling temperature, the fumes of the acid would rise and move into the shaft inside the condenser. The exit point of this shaft is covered with a silicon pipe with is placed inside a water bucket from the other end. If the fumes reached the top end of the shaft, they would move to water which would only contaminate the water. The purpose of this scheme is to protect the environment of the experiment from the highly corrosive and dangerous sulfuric acid fumes.

4.4.2.1 Parameters

The experiment was performed under the following parameters. The flask was filled with 98% concentrated sulfuric acid. The specimen was placed inside the flask and immersed inside the acid. Then, water flow was initiated to precool the system.

The flow was controlled by a valve and initially, the flow was set to a minimum to protect the glass. The heater was started from the PID controller and the temperature was set to 300℃. The sample was placed inside the boiling acid for 1 hour. As the temperature reached boiling temperature, the fumes started to rise in greater volume. To condense these fumes, the water flow was increased by valve.

Summary

In this chapter, detailed experimental processes are explained. Hastelloy X was cut into different dimensions using the low-speed diamond saw cutter. The prepared substrates were cleaned using ethanol and acetone. $MoSi_2$ source of 99.99% purity was used as target material for EBPVD onto Hastelloy X. The substrate temperature was set at 200℃ and sample rotation speed to 10 rpm. Moreover, a base pressure of 2×10^{-6} Torr was achieved for this coating process. The deposition rate was kept at 1.08Å/s by alternating the current. Surface morphology and topography were characterized by scanning electron microscopy (SEM) and atomic force microscopy (AFM), respectively. In the second part, RF magnetron sputtering was used to deposit SiC thin film on graphite. The substrate temperature was increased up to 300°C. Moreover, substrate rotation speed was kept at 10 RPM. The gas pressure of 3 Pascal was used along with RF power of 120 W. 900 nm Silicon carbide thin film was deposited in 2 hours. SiC slurry was prepared using the oxidized SiC powders along with PEG as a binder. Both the immersion and withdrawal speeds were set to 35mm/min. The sample stayed inside the solution for 30 seconds. This process was repeated five times and then the coated samples were dried at 100℃ in a drying oven. Surface morphology and structural analysis were characterized by Optical Microscopy (OM) and FTIR. Corrosion testing was carried out at both low and high temperatures. For low-temperature testing, the samples were immersed in 98% sulfuric acid at 60℃ and 120℃ for 4 and 2 hours respectively. The corrosion rate was measured using the weight loss method. The samples were weighed before and after the corrosion to measure weight loss. A new setup was devised for high-temperature corrosion testing. The sample was immersed in 98% sulfuric acid which was then brought to boiling temperature. The sample was placed inside a round bottom flask which was covered in glass wool and wrapped inside an electric heater. The heater has a maximum temperature limit of 500℃. Corrosion tests were performed for 1 hour and after testing, the sample was cooled overnight and then cleaned.

Chapter 5

Results and Discussion

5.1 $MoSi_2$ coated Hastelloy X via EB PVD

5.1.1 Corrosion Rate of bare and $MoSi_2$ coated Hastelloy X

Corrosion rates of all samples were calculated by the weight loss method. The Eq. 5-1 used for its calculation is given below [1]:

$$r = 8.76 \times 10^7 \left(\frac{W}{A \times T \times \rho}\right) \qquad \text{Eq. 5-1}$$

Where r is corrosion rate in μm/year, A is exposed surface area in cm^2, W is weight change of sample in grams, T is time in hours, and ρ is density in g/cm^3. The corrosion results of $MoSi_2$ coated Hastelloy X and bare Hastelloy X are given in Table 5-1 below.

Table 5-1 Corrosion results.

Sample ID	**Mass Change (g)**	**Surface Area (cm^2)**	**Temperature (℃)**	**Penetration Depth (mm/yr)**
SS-304	0.0206	17.42558	60	3.298029
Hastelloy X	0.0004	14.28299	60	-0.07461
$MoSi_2$ coated Hastelloy X	0.00036	10.0387	60	-0.09554
SS-304	0.0165	4.139928	120	22.23799

Hastelloy X	0.0131	14.6217	120	4.773925
$MoSi_2$ Coated Hastelloy X	0.0044	9.480924	120	2.472887
Hastelloy X	0.0567	2.903272	300	208.1266155
$MoSi_2$ coated Hastelloy X	0.00564	2.554156	300	23.53227817

Corrosion tests were performed at both low and high temperatures via the weight-loss method. Test coupons of bare Hastelloy X, SS-304, and $MoSi_2$ coated Hastelloy X was immersed in 98% sulfuric acid. At low temperatures, $MoSi_2$ coated Hastelloy X showed better corrosion resistance than bare HX and SS-304. Meanwhile, bare HX showed a high corrosion rate in boiling sulfuric, and $MoSi_2$ coated HX exhibited much better corrosion resistance.

5.1.2 Visual Inspection of corroded and uncorroded samples

Figure 5-1 shows the visual appearances of the specimens before and after exposure to 98 wt% sulfuric acid in different conditions. Hastelloy X (HX) showed slight weight gain at low temperatures. But when the test was performed at a temperature of 120℃, Hastelloy X showed weight gain and the corrosion rate increased significantly which was rated as a failure according to criteria given in [2]. This can be seen from the visual image of Hastelloy X in Figure 5-1 (c).

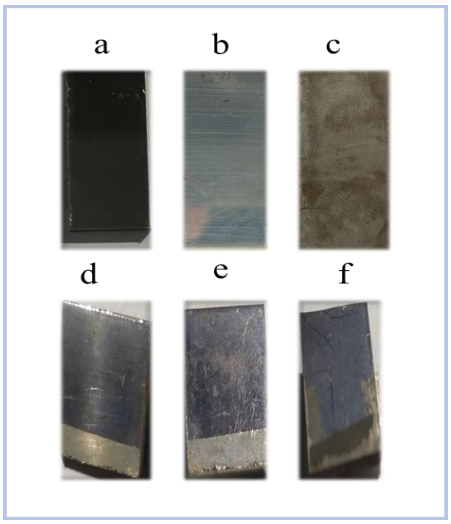

Figure 5-1 Visual appearance of specimens before and after exposure to 98 wt% sulfuric acid. (a) uncorroded HX (b) corroded HX at 60℃ (c) corroded HX at 120℃ (d) uncorroded $MoSi_2$ coated HX (MHX) (e) corroded MHX at 60℃ (f) corroded MHX at 120℃

Bare Hastelloy X showed slight discoloration at 60℃ as shown in Figure 5-1 (b) and complete discoloration at 120℃ in Figure 5-1 (c). Meanwhile, $MoSi_2$ coated HX showed no apparent change in coating but showed similar discoloration behavior on the non-coated portion [3].

5.1.3 Morphological analysis of corroded $MoSi_2$ coated Hastelloy X

Microscopic images were taken placing the sample under an optical microscope. Figure 5-2 shows the micrographs of uncorroded samples. An optical micrograph shows that $MoSi_2$ coating is uniform on the surface of the Hastelloy X substrate. The thickness of the coating is ~1 micron. Figure 5-2 (c) shows the edge of the coating on the substrate.

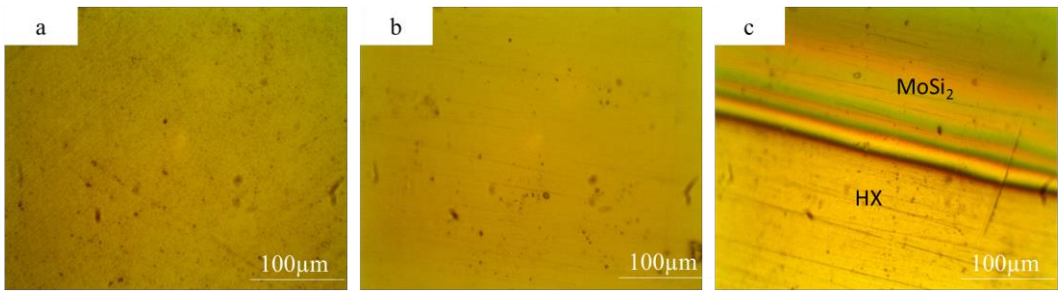

Figure 5-2 Optical micrographs of uncorroded specimens (a) Bare HX (b) Surface of MHX (c) Edge of MHX.

Figure 5-2 (a) shows the micrograph of the uncorroded Bare HX specimen before the corrosion test having a smooth surface with pores present. Figure 5-2 (b) and (c) indicates the micrographs of the surface and edges of the uncorroded $MoSi_2$ coated HX before the corrosion test, which indicates that the uncorroded specimen has a smooth coating with pores present in the Hastelloy X substrate.

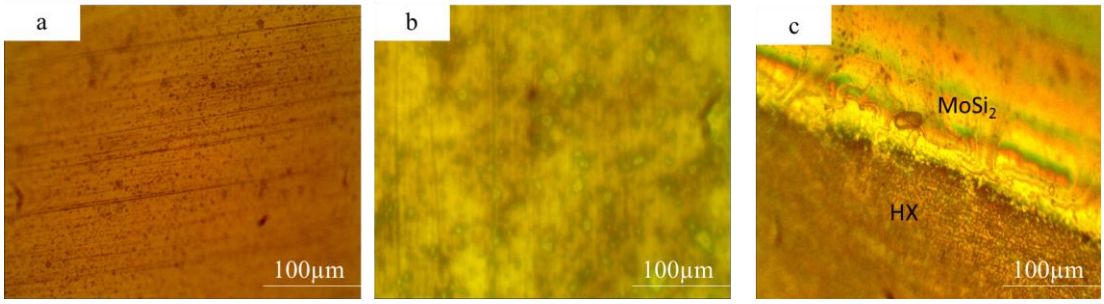

Figure 5-3 Optical micrographs of corroded specimens at 60℃ (a) Bare HX (b) Surface of MHX (c) Edge of MHX.

Figure 5-3 (a) shows the micrograph of the corroded Bare HX specimen at 60°C, the surface gets a bit rough slightly increasing the number of pores, but still, no significant change is seen in Bare HX including negligible mass change. Figure 5-3 (b) and (c) shows the surface of the $MoSi_2$ coated HX corroded at 60℃ for 4 hours. The coating was still intact. The rough surface of the $MoSi_2$ coated Hastelloy X is seen in the micrographs. The $MoSi_2$ coated samples show a slight change in corrosion rate at 60℃ than bare Hastelloy X [4].

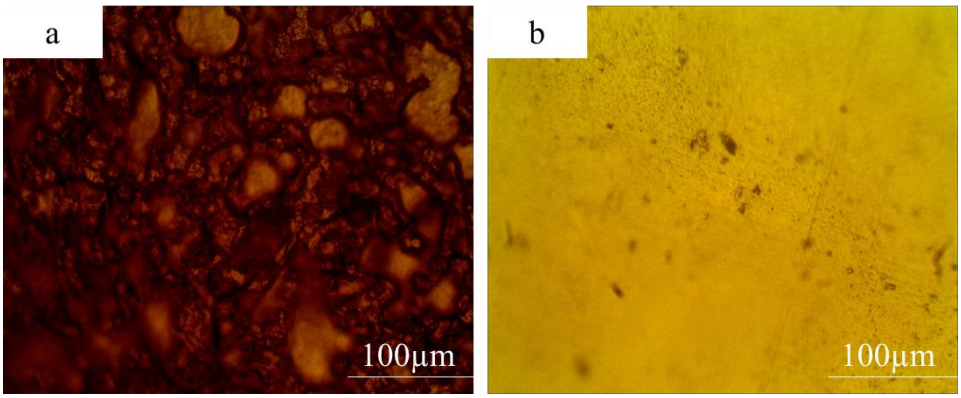

Figure 5-4 Optical micrographs of corroded specimens at 120℃ for 2hr. (a) Bare HX (b) Surface of MHX (c) Edge of MHX.

Figure 5-4 (a) shows the micrograph of the corroded Bare HX specimen at 120°C for 2 hours show a significant weight loss and high corrosion rate. The surface is much

rougher than the corrosion test done at 60℃ for 4 hours. The color of the specimen is dark. Bare HX showed a significant change in weight and the increment in corrosion rate is considered as a failure according to the criteria. Figure 5-4 (b) shows the surface of the $MoSi_2$ coated HX corroded at 120℃ for 2 hours. $MoSi_2$ coated Hastelloy X showed a much-improved corrosion rate at 120℃ than bare Hastelloy X. However, a slight weight change is seen while a significant decrease in surface area is seen. It shows that a portion of Hastelloy X without protective coating corroded. This explains the reason as concluded by Kubo et al. that silicon-containing ceramics are excellent contenders against sulfuric acid corrosion at high temperatures for a long time.

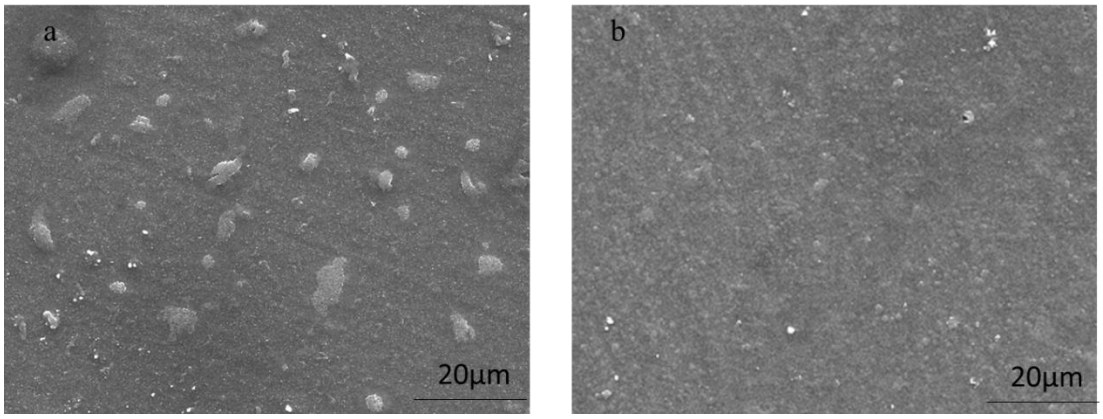

Figure 5-5 SEM images of Corroded $MoSi_2$ coated samples. (a) At 60℃ and (b) At 120℃.

In Figure 5-5 (a) small chunks can be seen on the surface of the $MoSi_2$ coating after being immersed in 98% sulfuric acid. Upon the EDX analysis of these chunks, as shown in Table 5-2, the elemental composition showed a significant increase in oxygen percentage. This also keeps in check with the corrosion rate, which was in negative value which implied oxidation [1].

Table 5-2 EDX results of $MoSi_2$ coated HX corroded at 60℃.

Element	Weight%	Atomic%
O K	49.40	66.70
Na K	2.36	2.22
Si K	11.75	9.04
S K	26.37	17.76
K K	3.52	1.95
Cr K	1.76	0.73
Fe K	1.32	0.51
Ni K	2.12	0.78
Mo L	1.39	0.31
Totals	100.00	

Figure 5-5 (b) depicts the surface morphology of the $MoSi_2$ coated sample at 120℃ in 98% sulfuric acid for 2 hours. The corrosion results show weight loss at this temperature and there are no chunks formed at this temperature. The surface was still intact and smooth. Upon the EDX analysis of the surface, the high oxygen content was reported as shown in Table 5-3. As reported in the literature, the formation of SiO_2 occurs due to the presence of silicon in the film. This layer protects the surface of the substrate from corrosion [5].

Table 5-3 EDX Analysis of $MoSi_2$ coated HX corrosion at 120℃.

Element	Weight%	Atomic%
O K	7.08	15.28
Si K	41.57	51.13
S K	7.77	8.37
Cr K	10.18	6.76
Fe K	8.33	5.15
Ni K	18.69	11.00
Mo L	6.38	2.30
Totals	100.00	

The thickness and surface roughness of the deposited film was analyzed by AFM [6]. For film thickness, the substrate was masked from one side. After the process the image from multiple places the mean difference between heights at the masked point and coated sample. The thickness of the film was calculated to be 360 nm as shown in Figure 5-6.

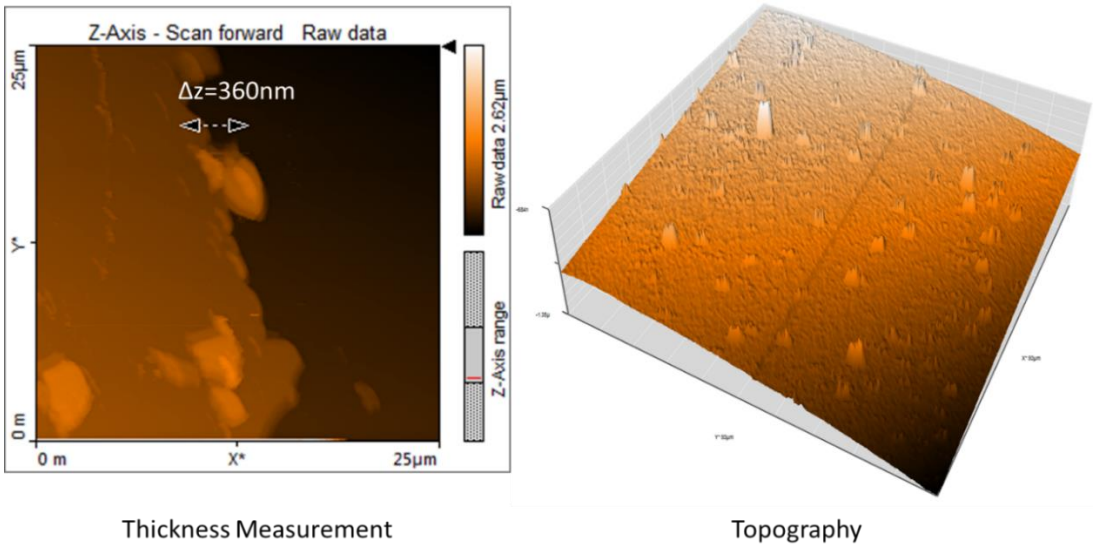

Figure 5-6 AFM images of $MoSi_2$ coated Hastelloy X. Thickness (left) and Topography (right).

The surface roughness of the coated sample was calculated to be 3.97 nm. The topography of the coated sample shows smoothness over the surface with peaks at some points. As indicated in the literature, the surface smoothness is related to deposition rate. The lower the deposition rate, the smoother the surface will be which is indicated by these sharp peaks [7].

5.1.4 Structural Analysis $MoSi_2$ coated Hastelloy X

Figure 5-7 shows the XRD patterns of Hastelloy X coated with $MoSi_2$ before and after corrosion at 60℃ and 120℃ in 98% sulfuric acid. A strong peak at 22 degrees was found in the range of 20-25 degrees in the sample which underwent corrosion at 60℃, which corresponds to silicon Si, which is a plain coated $MoSi_2$ sample, the same peak was reported in the literature [8-10]. Another strong peak at 43.7 degrees was found in the range of 40-45 degrees which represents the existence of $MoSi_2$ in all the samples, all peaks correspond to the presence of α-$MoSi_2$, same results were observed in the literature [10, 11]. Furthermore, a strong peak was observed in the range of 50-60 degrees in all three specimens which indicates the presence of Hastelloy X [4] as a substrate on the material, as the corrosion temperature difference varies from as-deposited to corrosion at 60° C the peak strengthens but after corrosion at 120° C the peak again shortens, in literature, similar peaks were observed [12].

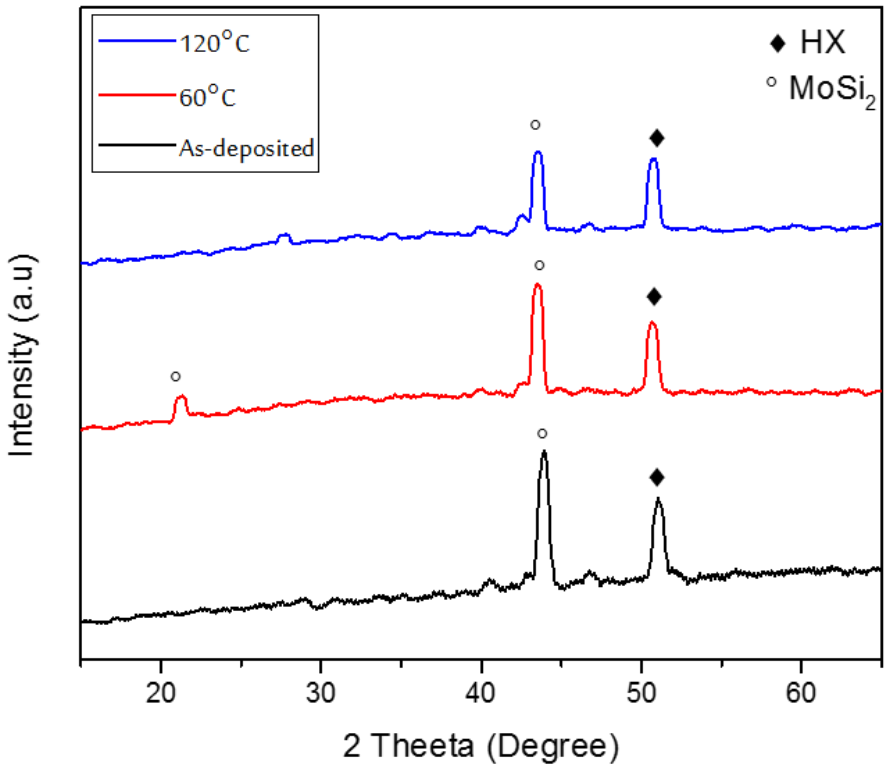

Figure 5-7 XRD Pattern of $MoSi_2$ coated Hastelloy X.

5.2 SiC/$MoSi_2$ coated Hastelloy X via RF magnetron sputtering

SiC was coated onto $MoSi_2$ coated HX via RF Magnetron sputtering. The as-deposited coupons were then annealed at 900℃ for 2 hours [4]. The sample then underwent corrosion at boiling temperature.

5.2.1 Corrosion rate of SiC/$MoSi_2$ coated Hastelloy X via RF magnetron sputtering

SiC/$MoSi_2$ coated HX samples were immersed in boiling sulfuric acid. The corrosion was measured using Eq. 5-1. The mass change, surface area, and corrosion rate are given in Table 5-4.

Table 5-4 Corrosion rate of $SiC/MoSi_2$ coated HX.

Sample ID	Mass Change (g)	Surface Area (cm^2)	Temperature (℃)	Penetration Depth (mm/yr)
$SiC/MoSi_2$ coated HX	0.00336	5.505336	300	6.504107882

$SiC/MoSi_2$ coated HX exhibited the most improved corrosion resistance at boiling temperature. The corrosion rates of bare HX, $MoSi_2$ coated HX and $SiC/MoSi_2$ coated HX was around 208.1, 23.5, and 6.5 mm/yr respectively. The corrosion resistance of $SiC/MoSi_2$ coated HX improved by around 96%.

5.2.2 Visual Inspection of corroded and uncorroded samples

Figure 5-8 shows the visual appearance of the $SiC/MoSi_2$ coated HX before and after being immersed in 98% sulfuric acid at 300℃. The figure shows slight discoloration around the edges of the coating. The coating remained intact in a highly corrosive environment [1].

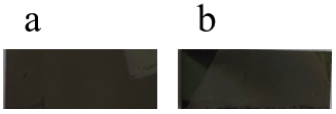

Figure 5-8 $SiC/MoSi_2$ coated HX (a) before corrosion and (b) after corrosion.

5.2.3 Morphological analysis of $SiC/MoSi_2$ coated Hastelloy X via RF magnetron sputtering

The optical micrographs of $SiC/MoSi_2$ coated HX can be seen in Figure 5-9. The as-deposited sample exhibits smooth surface coating with no crack or grain formation. When the sample is annealed at 900℃ for 2 hours in an inert environment, some coalescent particles are seen on the surface of the coated sample. This is in correspondence with [13]. Figure 5-9 c exhibits the surface morphology of the corroded sample after being immersed in 98% sulfuric acid at 300℃. The surface of both samples i.e. pre and post corrosion shows that the coating is still intact and there is no crack or void formation.

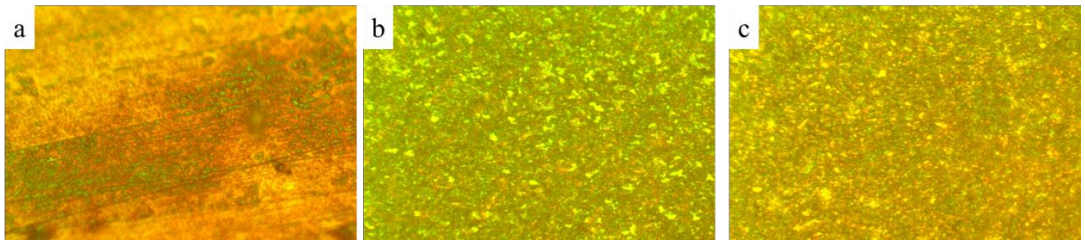

Figure 5-9 Optical micrograph of SiC/MoSi2 coated HX (a) as-deposited (b) annealed at 900℃ (c) after corrosion in boiling sulfuric acid

5.3 SiC Deposited Hastelloy X via Dip Coating

5.3.1 Corrosion rate of SiC coated Hastelloy X via dip coating

Corrosion rates of all samples were calculated by the weight loss method. The equation used for its calculation is Eq. 5-1. The corrosion rate of SiC coated Hastelloy X via dip-coating process is given in Table 5-5 below.

Table 5-5. Corrosion Rate of SiC coated Hastelloy X via Dip Coating.

Sample ID	**Mass Change (g)**	**Surface Area (cm^2)**	**Temperature (℃)**	**Penetration Depth (mm/yr)**
SiC Coated HX (Dip Coating)	0.00032	5.2827	120	0.322772349

SiC coated Hastelloy X exhibited minute weight change at 120℃ and was rated good according to corrosion criteria.

5.3.2 Morphological analysis of SiC coated Hastelloy X via dip coating

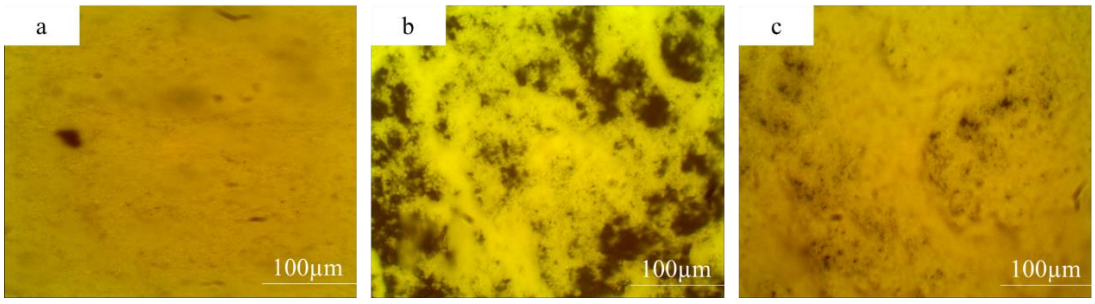

Figure 5-10 Optical Micrographs of SiC coated HX via Dip coating. (a) SiC coated HX (b) SiC coated HX annealed at 1000℃ for 2 hours (c) SiC coated HX after corrosion at 120℃.

Figure 5-10 displays the micrograph of SiC coated onto Hastelloy X via a dip-coating process. Figure 5-10 (a) provides the image of as-deposited SiC slurry onto the substrate. The coating seems to be less smooth than deposition via the PVD process. Figure 5-10 (b) displays the image of the SiC coated sample after being annealed at 1000℃ for two hours. The oxidation of substrate can be visualized from this image. Figure 5-10 (c) shows the corroded sample at 120℃ for 2 hours in 98% sulfuric acid. The image is in line with the results from the corrosion rate as this coating strongly resisted the highly corrosive acid.

5.3.3 Structural Analysis of SiC coated Hastelloy X via dip coating

FTIR spectroscopy was employed to analyze the structural analysis of SiC deposited films onto the Hastelloy X substrate by wet chemistry. Oxidized SiC powder was used in slurry preparation along with Polyethylene glycol (PEG), which was used as a binder. The peaks were identified according to the literature as shown in Table 5-6.

Table 5-6 FTIR peaks and ranges.

SiC deposition on HX As deposited				
Sr No.	**Range**	**Peak**	**Functional Group**	**Reference**
1	646.8-971.66	809.2	Si-C	[14-16]
2	1007.1-1148.7	1071	SiO_2	[15]
3	1148.7-1290.4	1219.6	$Si-CH_3$	[14]
SiC deposition on HX Annealed				
Sr No.	**Range**	**Peak**	**Functional Group**	**Reference**
1	689.18-979.4	809.2	Si-C	[14-16]
2	993.26-1297.33	1071	$Si-O_2$	[15]

The as-deposited specimen indicated the presence of a hydrogenated carbon group due to the presence of PEG. Meanwhile, the peaks of SiC and SiO_2 were identified in both specimens. After annealing at 1000℃, there is no sign of hydrogenated carbon over the surface of SiC coated Hastelloy X due to the evaporation of PEG. The SiC peak resembles the β-SiC phase. Figure 5-11 depicts the ranges of the peaks in the samples.

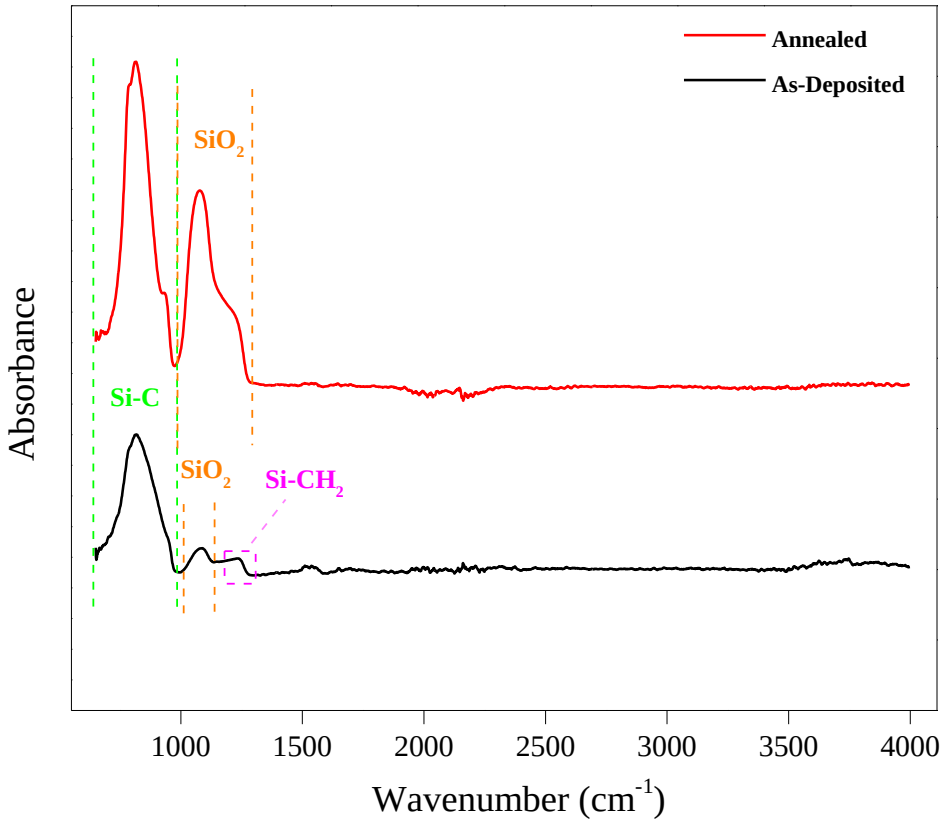

Figure 5-11 FTIR spectra of SiC coated HX (as-deposited and annealed).

Excellent quality $MoSi_2$ thin films were obtained through the EBPVD technique at 200℃ substrate temperature. The smoothness of the surface was measured by AFM along with thickness. The peaks of the deposited film were identified as α$MoSi_2$ and the substrate Hastelloy X. The samples exhibited a minute weight change at 60℃ but at 120℃ weight change increased significantly. Bare Hastelloy X at 120℃ rated as a failure. $MoSi_2$ coated Hastelloy X also showed corrosion. The $MoSi_2$ coated Hastelloy X showed improved corrosion resistance than bare HX as the corrosion resistance was improved by 48%. This was further confirmed by microscopic images which showed no change in morphology of the ceramic coating. The oxygen content increased significantly after corrosion as indicated by EDX analysis. SiC/$MoSi_2$ coated Hastelloy X via PVD showed the best corrosion rate at 300℃. The visual inspection indicated no discoloration of the specimen after the corrosion testing. The morphological analysis revealed that the coating remained intact after being immersed in 98% sulfuric acid at 300℃. SiC coated Hastelloy X via dip-coating showed the most improved corrosion resistance at 120℃. It showed no major change in mass loss as

confirmed by the surface morphology. SiC peaks were analyzed as-deposited and after annealing.

References

1. Tomar, S., et al., *Evaluation of materials of construction for the sulfuric acid decomposition section in the sulfur–iodine (S–I) cycle for hydrogen production: Some preliminary studies on selected materials.* 2019. **131**(9): p. 1-8.
2. Kubo, S., et al., *Corrosion resistance of structural materials in high-temperature aqueous sulfuric acids in thermochemical water-splitting iodine–sulfur process.* International Journal of Hydrogen Energy, 2013. **38**(16): p. 6577-6585.
3. Kubo, S., et al., *Corrosion resistance of structural materials in high-temperature aqueous sulfuric acids in thermochemical water-splitting iodine–sulfur process.* 2013. **38**(16): p. 6577-6585.
4. Park, J.-W., et al., *Materials development for process heat exchanger (PHE) in nuclear hydrogen production system.* Nuclear Engineering and Design, 2014. **271**: p. 318-322.
5. Corgnale, C., M.B. Gorensek, and W.A.J.P. Summers, *Review of Sulfuric Acid Decomposition Processes for Sulfur-Based Thermochemical Hydrogen Production Cycles.* 2020. **8**(11): p. 1383.
6. Wang, R., et al., *Using Atomic Force Microscopy to Measure Thickness of Passive Film on Stainless Steel Immersed in Aqueous Solution.* Scientific Reports, 2019. **9**(1): p. 13094.
7. Shan, Y., X. He, and J.J.J.O.F.M. Xu, *Effects of deposition rate on surface topography of Ni-Cr thin film deposited by EB-PVD.* 2007. **38**(2): p. 249.
8. Zhang, Y., et al., *Effect of hot-dip siliconizing time on phase composition and microstructure of Mo–MoSi2 high temperature structural materials.* 2019. **45**(5): p. 5588-5593.
9. Chen, P., et al., *Preparation of oxidation protective MoSi2–SiC coating on graphite using recycled waste MoSi2 by one-step spark plasma sintering method.* 2019. **45**(17): p. 22040-22046.
10. Han, X.-x., et al., *Microstructure, sintering behavior and mechanical properties of SiC/MoSi2 composites by spark plasma sintering.* 2018. **28**(5): p. 957-965.
11. Mohamad, A., et al., *Thermal and Mechanical Properties of α-MoSi2 as a High-Temperature Material.* 2018. **255**(4): p. 1700448.
12. Ekambaram, P.J.J.o.M.R. and Technology, *Study of mechanical and metallurgical properties of Hastelloy X at cryogenic condition.* 2019. **8**(6): p. 6413-6419.
13. Park, J.-W., et al., *A surface modification of Hastelloy x by a SiC coating and an ion beam irradiation for a potential use for iodine-sulfur cycle in nuclear hydrogen production system.* 2008. **1125**.
14. Kaneko, T., et al., *FTIR analysis of a-SiC:H films grown by plasma enhanced CVD.* Journal of Crystal Growth, 2005. **275**(1): p. e1097-e1101.
15. Rajarao, R. and V. Sahajwalla, *A cleaner, sustainable approach for synthesising high purity silicon carbide and silicon nitride nanopowders using macadamia shell waste.* Journal of Cleaner Production, 2016. **133**: p. 1277-1282.
16. Jiang, S., et al., *Study on the synthesis of β-SiC nanoparticles from diamond-wire silicon cutting waste.* 2019. **9**(41): p. 23785-23790.

Chapter 6

Conclusions and Recommendations

6.1 Conclusions

1. Excellent quality $MoSi_2$ coated Hastelloy X thin films were obtained as a result of Electron beam physical vapor deposition (EB PVD). Superior quality SiC coated Hastelloy X with $MoSi_2$ as an intermediate layer was attained as a result of RF magnetron sputtering. A non-uniform SiC film was obtained from Dip coating of SiC slurry. All three coated thin films showed good adhesion with the substrate.
2. Both bare Hastelloy X and $MoSi_2$ coated Hastelloy X showed weight gain at 60℃. Both $MoSi_2$ and bare Hastelloy X exhibited weight loss at 120℃. $MoSi_2$ coated Hastelloy X showed improved corrosion resistance at 120℃ than Hastelloy X. The improvement was about 48%. SiC coated Hastelloy X showed the most improved corrosion resistance at 120℃.
3. At boiling temperature, SiC/$MoSi_2$ coated Hastelloy X showed the most improved corrosion resistance by 96%. Meanwhile, the corrosion resistance of $MoSi_2$ coated Hastelloy X improved by ~89%. It is concluded that SiC coated Hastelloy X with $MoSi_2$ as an intermediate layer can be a potential candidate as a structural material for PHE in the I-S cycle.

6.2 Future recommendations

1. Testing of coated samples in an SO_2/SO_3 environment at a temperature above 800℃ could be done in the future.
2. Design and modeling of SiC coated Hastelloy X using $MoSi_2$ as an interlayer could be done to identify effective heat transfer configuration in the sulfuric acid decomposition stage.

Appendix A

Corrosion Behavior of $MoSi_2$ Coated Hastelloy X for Iodine -Sulfur Cycle for Hydrogen Production

Zain Hussain[1], Zuhair S Khan*, Asghar Ali, Nisar Ahmed, Wajahat Qasim, Altamash Shabbir
U.S.-Pakistan Center for Advanced Studies in Energy, National University of Sciences and Technology, Islamabad 44000, Pakistan.
Presenting author email: zhussaintee19.ces@student.nust.edu.pk
***Corresponding author: zuhair@uspcase.nust.edu.pk**

Abstract

The iodine-sulfur cycle is a three-step thermochemical reaction in which sulfuric acid is decomposed at high temperatures to produce hydrogen. Sulfuric acid decomposition stage requires materials which can withstand highly corrosive environment at relatively high temperature. Suitable anticorrosive and high temperature tolerant materials are required to realize an efficient iodine-sulfur cycle. Hastelloy X is a Ni-Cr-Fe-Mo based alloy that has exceptional combination of high temperature tolerance and oxidation resistance; however, it presents challenges when subjected to sulfuric acid at elevated temperatures. Necessary protective coating is required to extend its durability. In this regard, SiC has excellent corrosion resistance and may be coated over Hastelloy X against sulfuric acid; however, the mismatch between the coefficient of thermal expansion (CTE) of Hastelloy X, which equals 16×10^{-6} °C^{-1} at 1000 °C and that of SiC, which equals 5×10^{-6} °C^{-1} is the basic impediment to materialize this concept. An interlayer of appropriate CTE is required to compensate for this mismatch. In this regard, $MoSi_2$ which has a CTE of 8.5×10^{-6} °C^{-1} at 1000 °C, can serve as an excellent interlayer. In this work, we choose $MoSi_2$ as an intermediate layer to provide good bonding between the top SiC and the Hastelloy X substrate as well as excellent anticorrosion properties. The $MoSi_2$ thin films were deposited via electron beam physical vapor deposition (EBPVD) method, followed by SiC deposition via RF magnetron sputtering. Corrosion tests were performed at (60°C and 120°C) in 98% sulfuric acid using the weight-loss method. The samples were immersed inside the acid at 60°C (4 hours) and 120°C (2 hours), respectively. Bare Hastelloy X showed a slight weight gain at 60°C and a weight loss at 120°C. The $MoSi_2$ coated

Hastelloy X showed weight gain at 60℃ and a weight loss at 120 ℃. The weight gain is the result of oxides formation whereas, weight loss may be attributed to corrosion due to H^+ ions. Corrosion behavior of $MoSi_2$ coated HX will be presented in this paper. Corrosion behavior of SiC over $MoSi_2$ will be presented in the future.

Keywords: Iodine-sulfur cycle, Corrosion, E-beam Evaporation, SiC, $MoSi_2$.